Recent developments in Earth-abundant copper-sulfide thermoelectric materials

Article

Accepted Version

Recent Developments in Earth-Abundant Copper-Sulfide Thermoelectric Materials

Anthony V Powell*

Department of Chemistry, University of Reading, Whiteknights,

Reading RG6 6AD, UK

Abstract

The ability of thermoelectric devices to convert waste heat into useful electrical power has stimulated a remarkable growth in research into thermoelectric materials. There is however, growing recognition that limited reserves of tellurium together with the reduction in performance that occurs at elevated temperatures, places constraints on the widespread implementation of thermoelectric technology based on the current generation of telluride-based devices. Metal sulfides have attracted considerable attention as potential tellurium-free alternatives. This perspective provides an overview of the key characteristics of sulfide thermoelectrics and the advantages they offer in the development of devices for energy recovery in the temperature range $373 \leq T/K \leq 773$. The structures and properties of a group of synthetic materials, related to the minerals chalcocite (Cu_2S), stannite (Cu_2FeSnS_4) / kesterite (Cu_2SnS_4), chalcopyrite ($CuFeS_2$), bornite (Cu_5FeS_4), colusite ($Cu_{26}V_2(As,Sn,Sb)_6S_{32}$) and tetrahedrite ($(Cu,Fe)_{12}Sb_4S_{13}$), are discussed. In addition to all being composed of Earth-abundant elements, these sulfides share a common tetrahedral CuS_4 structural building block. The use of chemical substitution to manipulate electrical and thermal transport properties is described and common features are identified. This includes the presence of low-energy vibrational modes, the onset of copper-ion mobility and the emergence of a liquid-like sub-lattice, which serve to reduce thermal conductivity. Issues associated with materials' stability during synthesis, consolidation and device operation, due to sulfur volatilization and migration of mobile copper ions are also highlighted. Future prospects for sulfide thermoelectrics are discussed in the light of the performance of materials investigated to date.

*E-mail:a.v.powell@reading.ac.uk

1 Introduction

Thermoelectric devices afford the capacity to convert otherwise waste heat, much of which is generated by combustion of fossil fuels, into useful electrical energy. Thermoelectric energy harvesting therefore has the potential to reduce fossil-fuel consumption by increasing the overall efficiency of the process, thereby contributing to reducing the emission of greenhouse gases. Significant sources of waste heat include the manufacturing industries, particularly those associated with steel, glass or cement production and propulsion units in the automotive, marine and aviation sectors. For example, 60 - 70 % of energy in an automotive internal-combustion engine is rejected as heat. Thermoelectric energy recovery may also be exploited in lower temperature applications, including powering microelectronic devices and sensors from body heat, solar thermal collection in industrial buildings, geothermal sources and cooling-water streams in the nuclear industry.

The efficiency of a thermoelectric device is determined by the performance of the component materials, as embodied in the dimensionless figure-of-merit (Eq. 1) comprising the Seebeck coefficient (S), electrical (σ) and thermal (κ) conductivities.

$$ZT = \frac{S^2 \sigma T}{\kappa} \qquad \text{Eq. 1}$$

High-performance requires a high electrical conductivity, typically found in metallic phases, to be combined with a large Seebeck coefficient: a characteristic more usually associated with a non-metallic material. Furthermore, the thermal conductivity has contributions from both lattice vibrations (κ_L) and charge carriers (κ_e). The latter is linearly related to the electrical conductivity through the Wiedemann-Franz law.

The Seebeck coefficient, electrical conductivity and thermal conductivity all show a dependence on the charge-carrier concentration; high Seebeck coefficients occur at carrier concentrations where the electrical and thermal conductivities are low and vice-versa. Consequently, the three contributions to the figure-of-merit cannot be independently optimised and a degree of compromise is required to achieve high-performance. The highest performance generally occurs for carrier concentrations in the range 10^{19} - 10^{21} cm^{-3}: the regime of heavily-doped semiconductors.

A thermoelectric device consists of an array of pairs of *n*- and *p*-type semiconductors (Figure 1) connected electrically in series and thermally in parallel. Current commercial devices are

composed of Bi_2Te_3, suitably doped to produce *n*- and *p*-type variants. A Bi_2Te_3 device has a figure-of-merit that approaches unity at temperatures in the range $350 \leq T/K \leq 450$. Although widely used in niche applications, there are a number of disadvantages associated with Bi_2Te_3-based devices. In particular, the figure-of-merit decreases significantly at higher temperatures and the component materials melt at *ca*. 853 K, rendering such devices unsuitable for applications involving high-grade waste heat. Moreover, there are concerns surrounding the sustainability of a tellurium supply sufficient for large-scale implementation of thermoelectric technology, as outlined in Section 2 below. These factors have provided the motivation to extend the search for high-performance thermoelectric materials beyond tellurides. In recent years, this has led to investigation of a spectrum of alternative materials, including chalcogenides,[1] oxy-chalcogenides,[2] oxides,[3] skutterudites,[4] Half-Heusler phases,[5] Zintl phases,[6] magnesium pnictides,[7] clathrates,[8,9] silicon-germanium alloys[10] and metal silicides.[10]

The difficulties inherent in maximising ZT due to the inter-dependence of S, σ and κ, have led to the development of a number of design strategies for the creation of high-performance materials,[11] many of which seek to achieve a degree of separation between electrical and thermal contributions to ZT. These include the introduction of species with low-energy localised vibrational modes (the phonon-glass electron crystal (PGEC) approach),[12] the formation of nanoinclusions[13] or nanocomposites,[14] grain-boundary engineering,[15] low dimensionality,[16] band structure modifications including the creation of resonant states,[17] energy filtering,[18] exploiting magnetic interactions to increase the carrier effective mass,[19] increasing the power factor through spin fluctuations of itinerant electrons[20] and the phonon-liquid electron-crystal (PLEC) approach.[21]

Judicious application of these design strategies has led to some outstanding increases in the figure-of-merit of non-telluride phases, for which ZT = 1.0 is now routinely exceeded. For example the *n*-type, triply-filled skutterudite, $Ba_{0.08}La_{0.05}Yb_{0.04}Co_4Sb_{12,}$ exhibits ZT = 1.7 at 850 K,[22] while the *p*-type material $Cu_{2-x}Se$ reaches ZT = 1.5 at 1000 K.[21] Improvements in performance have resulted from the increased understanding that has emerged of the impact of structural features across multiple length scales on electrical and thermal transport properties. This has resulted in an evolution from what have been termed[23] first-generation materials with $ZT \approx 1.0$ through a second generation, in which nanostructuring increases the figure-of-merit to $ZT \approx 1.5$, to a third generation where multiple design strategies are applied

simultaneously, leading to ZT ≈ 2.0. Even higher figures-of-merit have been achieved in apparently simple materials such as SnSe, for which ZT = 2.6 at 923 K has been reported,[24] albeit in a specific direction in a single crystal.

The majority of thermoelectric materials typically show a maximum figure of merit within a relatively narrow temperature range; the average value over the temperature profile of the device being much lower. In addition, materials such as SnSe exhibit the highest figure-of-merit following a temperature-induced phase transition. The values in the low temperature region are much reduced, which again reduces the average ZT over the temperature range of operation. In the majority of the non-telluride materials the high figures-of-merit are achieved at comparatively high temperatures, typically in excess of 800 K. However, it has been estimated[25] that *ca*. 80 % of industrial waste heat is released at temperatures in the range 373 ≤ T/K ≤ 573, a region where the performance of many of the high-performance non-tellurides is more modest. For example, whilst the optimally-doped Zintl phase, $Yb_{14}Mn_{1-x}Al_xSb_{11}$ exhibits ZT = 1.2 at 1223 K,[26] this reduces to ZT ≈ 0.4 at 550 K. There continues to be something of a dearth of materials suitable for applications at these intermediate temperatures.

This perspective outlines recent developments in a group of metal sulfides containing Earth-abundant elements that show promise for applications in energy recovery in the mid- to intermediate temperature range, including the region where the highest proportion of industrial waste heat is released. The nature of a perspective means it is somewhat selective in coverage. It is not the intention to provide a comprehensive survey of thermoelectric materials, or even of metal sulfide thermoelectrics, for which there are a number of recent reviews. [27,28,29,30,31] The focus is on a sub-set of metal sulfides, whose structures contain the tetrahedral CuS_4 building block, in which motion of the copper ions, either in the form of localised vibrational modes or outright diffusion has a significant impact on thermoelectric performance.

2 Sulfides as Thermoelectric Materials

Perhaps the most striking feature to emerge from a comparison of the chalcogens, S, Se and Te (Table 1) is the terrestrial abundance of sulfur, which is 4 - 5 orders of magnitude greater than that of its heavier congeners. Indeed, tellurium has been identified as one of the top 9 “at

risk" elements[32] and as a critical mineral by the US Government.[33] In addition to its greater abundance sulfur has a much greater availability, being present in the native form and mineral ores, as well as being recoverable from fossil-fuel reserves. This contrasts with the position of tellurium and selenium, both of which are generally obtained as by-products of other processes. In addition, other technologies compete for these scarce resources. For example, it is estimated that 40 % of global tellurium production is used in the solar industry,[33] with thermoelectric devices being the next largest consumers at 30 %. Given the relatively modest reserves, a large increase in demand for tellurium from either of these sectors is not sustainable. The greater abundance and availability of sulfur is also reflected in a cost per kg that is a small fraction of that of selenium or tellurium. Collectively these factors impose restrictions on the wide-scale implementation of a telluride-based thermoelectric technology, necessitating the development of alternative materials containing more Earth-abundant elements.

Health and safety considerations are also important if the adoption of thermoelectric technology is to become widespread. Although data for the elements are of limited utility in this regard, since it is the bioavailability in a given compound that determines toxicity and environmental impact, the toxicity of solid-state chalcogenides relevant to thermoelectric phenomena, broadly mirrors that of the elements. For example the time-weighted-average (TWA) exposure limit of the binary Cu_2Q phases, with Q = Se, Te, is identical to that of the elements, while the analogous sulfide is not considered hazardous. The relatively low melting and boiling points of sulfur are potentially problematic in materials synthesis and with respect to stability under the conditions at which thermoelectric devices operate, owing to the volatility of sulfur. Although the higher atomic vibrational frequencies associated with the lighter sulfur atom, present challenges in achieving the low thermal conductivities that are attained in materials with high atomic masses, as will be described below, the unique characteristics of sulfides can be exploited to create materials with exceptionally low thermal conductivities.

Although the band structures of chalcogenides depend on the detailed structure and the identity of the cations present, elementary bonding considerations[34] suggest the decrease in electronegativity on going from sulfur to tellurium raises the energy of the anion valence orbitals (Figure 2), thereby decreasing the band gap (E_g). This is evidenced by electronic structure calculations on copper chalcogenides,[35] which reveal that the band gap of Cu_2S (0.299 eV) is greater than that of Cu_2Se (0.130 eV), while E_g disappears completely in the

corresponding metallic telluride. The reduction in electronegativity, coupled with an increase in atomic radius and atomic mass on going from S to Te, also results in a less ionic interaction with cation orbitals. A reduction in the energy separation between anion and cation orbitals also leads to more effective orbital overlap and a broadening of the bands (Figure 2). Broader bands imply a lower carrier effective mass (m^*), increasing mobility and facilitating conduction. Conversely, a larger energy difference between cation and anion orbitals, results in a narrowing of bands, an increase in m^* and more cationic character to the conduction band (CB), while the valence band (VB) assumes greater anionic character. This suggests that for sulfides, which for a given structure type have the largest band gaps of the three chalcogens, partial substitution of sulfur with a less electronegative anion offers a means of tuning m^* of the holes.

Although the polarizability of the di-anion increases between S and Te, the polarizability of S^{2-} remains high, comparable with that of the larger, heavier Se, and more than a factor of two greater than that of its lighter congener, O^{2-} (3.88×10^{-24} cm^3) or neighbour Cl^- (3.66×10^{-24} cm^3). A high polarizability favours anisotropic bonding, which in extreme cases leads to low-dimensional structures that offer advantages for achieving high thermoelectric performance, whilst a polarizable anion sub-lattice also facilitates cation diffusion.

Table 1: Key Parameters for the Chalcogens, Q = S, Se, Te

Q	**S**	**Se**	**Te**
Atomic weight	32.065	78.971	127.60
Melting point/°C	115.4	221	449.65
Boiling point/°C	444.72	685	988
Availability	Native form, recovered from natural gas and oil, several mineral sources	By-product of electrolytic copper refining, some mineral sources	Recovered from electrolytic refining of copper
Terrestrial Abundance /ppb	3.50×10^5	50	1
Annual Production/ metric tonnes[a]	8.0×10^4	2.80×10^3[c]	4.40×10^2[c]
Estimated Reserves/ metric tonnes[a]	$> 6.0 \times 10^{11}$	9.9×10^4	3.1×10^4
Cost per kg/US $[a]	0.15	44	82
Hazard Information[b]	Skin irritation (Category 5)	Acute toxicity, Inhalation (Category 3)	Acute toxicity, Inhalation (Category 4)
Time-weighted average exposure limit/ mg m^{-3}[b]	Not established	0.1	0.1
Electronegativity	2.58	2.55	2.10
Radius of Q^{2-}/Å	1.84	1.98	2.21
Polarizability of Q^{2-}/ 10^{-24} cm^3	10.2	10.5	14.0

[a]Data taken from U.S. Geological Survey 2019.[33]

[b]Hazard information taken from chemical suppliers Safety Data Sheets.

[c] Excludes US production.

All remaining data taken from the CRC Handbook of Chemistry and Physics.[36]

3 Structural Features of Copper Sulfides Derived from CuS_4 Tetrahedra

The CuS_4 tetrahedron serves as the building block for a variety of ternary and higher-order copper sulfides. Although simple vertex linking of CuS_4 tetrahedra would give rise to the zinc blende structure of 1:1 stoichiometry, CuS adopts the more complex covellite structure,[37] in which both $(S_2)^{2-}$ and S^{2-} species may be identified. However, the zinc blende network of vertex-linked tetrahedra (Figure 3) serves as the prototype for many ternary and quaternary copper sulfides, in which cation ordering results in the formation of supercells.

Materials of general formula, Cu*M*S_2 (*M* = Fe, Al , Ga, In, Tl) adopt the chalcopyrite structure of $CuFeS_2$, in which there is ordering of copper(I) and iron(III) cations over 4-coordinate sites, corresponding to a network of vertex-linked CuS_4 and FeS_4 tetrahedra (Figure 3). Cation ordering results in a doubling of the *c*-axis and a reduction from cubic to tetragonal symmetry - space group: $I\bar{4}2d$. Replacement of one half of the iron cations by tin, produces the stannite structure exemplified by Cu_2FeSnS_4 ($I\bar{4}2m$) in which CuS_4, FeS_4 and SnS_4 tetrahedra are linked through their vertices (Figure 3). Cation ordering again results in a doubling of the *c*-axis relative to that of the zinc-blende structure. Closely related to the stannite structure is that of kesterite (Figure 3). Although this also exhibits an $a_p \times a_p \times 2a_p$ superstructure, the symmetry is lowered to ($I\bar{4}$). These two structures are adopted by a range of quaternary sulfides of general formula Cu_2ABS_4, where *A*(IV) is drawn from group 14 (Si, Ge, Sn) and *B*(II) is a transition-series (Mn, Fe, Co) or group 12 (Zn Cd, Hg) cation. The stannite and kesterite structures differ in the manner in which cations are ordered. In the former, copper cations are located only in planes at z = 0.25 and 0.75 (4*d* sites), whereas in the kesterite structure they are found within every cation plane (2*a* and 2*c* sites). Materials containing transition-series cations appear to adopt the stannite structure. However, there is greater ambiguity surrounding materials such as Cu_2ZnSnS_4,[38,39] the origin of which is associated with the comparable X-ray scattering powers of the constituent cations, the similar unit cell parameters and the identical systematic absences of the space groups $I\bar{4}2m$ and $I\bar{4}$. Recent powder neutron diffraction and computational studies appear to confirm that Cu_2ZnASS_4 (*A* = Ge, Sn) adopt the kesterite structure along with the analogous selenides.[40,41]

The hypothetical zinc blende structure of vertex-linked CuS_4 tetrahedra generates a network of vacant tetrahedral sites. Complete occupation of these would produce the anti-fluorite structure of formula, Cu_2S (Figure 3). At high temperatures, Cu_2S does indeed adopt this cubic structure, in which Cu(I) cations are located in tetrahedral sites within a face-centred-

cubic array of sulfide anions, resulting in CuS_4 tetrahedra sharing both edges and faces. However, the structural chemistry of chalcocite Cu_2S is surprisingly complex.[42] At room temperature, it adopts a monoclinic distortion of a hexagonal-close packed anion array, containing 48 formula units per unit cell, with copper cations displaced to three coordinate sites. This converts to a hexagonal form on heating above 377 K, before the cubic phase appears above 743 K. Further structural complexity is introduced by the ability of Cu_2S to accommodate vacancies on the cation sub-lattice.[43] At room temperature, phases $Cu_{2-x}S$ adopt the djurleite structure in the range $0.04 \leq x \leq 0.07$ and the digeinite structure at $x = 0.2$. At intermediate compositions, mixtures of phases are formed, while each structure type also shows temperature-induced phase transitions, with all compositions exhibiting an anti-fluorite-type structure at high temperature, in which there is a statistical distribution of copper cations and vacancies over tetrahedral sites.

The Earth-abundant mineral bornite, Cu_5FeS_4, also adopts a cation-deficient anti-fluorite-type structure at high temperature (Figure 4), analogous to that of α–chalcocite, with two cation vacancies per unit cell.[44,45] The vacancies, together with copper and iron cations, are statistically distributed over the eight available tetrahedral sites. Vacancy ordering on cooling results in structures in which zinc blende (ZB)- and anti-fluorite (AF)-type sub-cells coexist (Figure 4). Below 540 K the cubic 2a phase[46] is formed in which the unit cell is doubled in each direction, due to alternation of the two sub-cells, whilst below 460 K, the orthorhombic (*Pbca*) 4a structure[47] is adopted. AF and ZB sub-cells again alternate in each direction in the 4a structure, but the vacancy ordering in the ZB sub-cells is inverted on progressing along the *b*-axis (Figure 4). This results in a structure with lattice parameters related to those of the high-temperature structure (a_p) by $4a_p \times 2a_p \times 2a_p$. A further first-order structural phase transition has been identified at sub-ambient temperatures.[48]

Further structural complexity is observed in copper-containing minerals. From a thermoelectric perspective, materials related to colusite[49] $Cu_{26}A_2B_6S_{32}$ (*A* = V, Nb, Ta; *B* = Ge, Sn) and tetrahedrite[50] $Cu_{10}A_2B_4S_{13}$ (*A* = Mn, Fe, Co, Ni, Zn, Cu, Hg, Cd; *B* = As, Sb, Bi) have been at the forefront of developments in sulfide thermoelectrics in recent years. The structure of colusite can be considered as a network of vertex-linked CuS_4 and BS_4 tetrahedra (Figure 5a) forming a zinc-blende-like network, with an enlarged $2a_p \times 2a_p \times 2a_p$ unit cell due to ordering of copper and *B*-type cations. Additional group 5 (*A*) cations are located in 1/16 of the remaining tetrahedral interstices, in an ordered fashion, such that they adopt a

body-centred cubic arrangement (Figure 5b), generating a complex structure in which metal-centred tetrahedra share both vertices and edges.

The crystal structure of tetrahedrite (Figure 6) is often considered as a complex defective derivative of that of zinc blende.[50] However, in contrast to the materials already discussed, transition-metal cations occupy both tetrahedral and trigonal planar sites, while pnictogen atoms are located at sites of trigonal-planar coordination. An alternative structural description that has been proposed[51] is in terms of a collapsed sodalite-type framework of transition-metal-centred tetrahedral centres (Figure 6b), in which CuS_3 trigonal pyramids are located in each of the hexagonal windows of the cage, while the cages are filled by sulfide anions, octahedrally coordinated to six trigonal planar CuS_3 ions to create a "spinner" (Figure 6c) This structural description reveals some similarities with those of cage-based PGEC-type, thermoelectric materials, such as skutterudites and clathrates.

4 Recent Advances in Copper Sulfide Thermoelectrics

A common feature of the structure types outlined above is a VB derived from hybridization of Cu(3*d*) and S(3*p*) orbitals. The generally high degeneracy of the VB results in relatively high Seebeck coefficients and thus power factors ($S^2\sigma$)[52] in several of the copper sulfides. Furthermore, there is appreciable copper-ion mobility in many of the more complex structures. This may manifest itself either in relatively large atomic displacement parameters, signifying pronounced vibrational motion about a crystallographic site, or may lead to delocalization of copper ions, leading to the copper sub-lattice attaining a liquid-like state, with a marked impact on thermal conductivity.

4.1. Materials Containing a Network of Vertex-Linked Tetrahedra

4.1.a Chalcopyrite-Related Phases

Chalcopyrite, $CuFeS_2$, affords a rare example of an *n*-type sulfide thermoelectric material. The naturally occurring material exhibits relatively modest thermoelectric properties,[53,54,] although copper-rich mineral samples, $Cu_{1+x}Fe_{1-x}S_2$, exhibit large *n*-type Seebeck coefficients (up to $|S| = 713\ \mu V\ K^{-1}$ at 300 K), analogous to their synthetic counterparts. Interaction of the charge carriers with the magnetic moment of Fe^{3+} plays a role and the S(T) behaviour can be described in terms of electron-magnon scattering to *ca*. 200 K. It has been shown

experimentally[55] and by first-principles electronic structure calculations[56,57] that the origin of the large Seebeck coefficient can be traced to the heavy-effective-mass conduction band. However, this reduces mobility, necessitating increases in carrier concentration to improve the electrical conductivity, which in turn decreases the Seebeck coefficient. Calculations suggest that optimally doped $CuFeS_2$ with an average grain size $d \approx 20$ nm, to reduce thermal conductivity, would exhibit ZT = 0.8 at 700 K.[55]

The impact of carrier doping on the thermoelectric properties of $CuFeS_2$ has been explored[58,55] through adjustments to the Cu:Fe ratio or by partial substitution of zinc at the copper site. Although precipitation of the binary phases, FeS_2 and ZnS leads to deviations from nominal stoichiometries, both *n*-type behaviour and the chalcopyrite structure are retained in $Cu_{1-x}Fe_{1+x}S_2$ (x = 0.03, 0.05) and $Zn_{0.03}Cu_{0.97}FeS_2$. Whilst doping reduces the Seebeck coefficient by *ca*. 40% at 400 K, it remains high for the comparatively low resistivity that is achieved, with the result that power factors are increased by a factor of approximately five from that of the undoped phase. Although carrier-doping also reduces the thermal conductivity from the relatively high value of $\kappa = 9.3$ W m^{-1} K^{-1} in $CuFeS_2$, the resulting value of $\kappa \approx 6$ W m^{-1} K^{-1} restricts the maximum figure-of-merit to ZT = 0.07 at 400 K, despite the high power factors. Interestingly, the presence of a magnetic ion (Fe^{3+}) enhances the carrier mass (to $3.5m_0$ - $5.6m_0$) through interaction with the magnetic moment and may offer an alternative approach to increasing the power factor. The magnetic ion also serves to scatter charge carriers, as evidenced in the differences in behaviour between the iron-excess materials and the zinc-substituted phase, which shows higher carrier mobility. At higher temperatures the electrical properties are retained and ZT is increased to 0.12 at 700K,[59] although the thermal conductivity remains high. While techniques such as high-pressure torsion to introduce defects and dislocations leads to significant reductions in thermal conductivity of 50 -70 % at room temperature, this is at the expense of impaired electrical transport properties.[60] Recent theoretical work[61] suggests that the experimentally studied compositions with *ca.* 3% doping, may not represent the optimum doping level and an increase in power factor by a factor of 2.5 is predicted at lower doping levels (< 1%). However, discrepancies between the Seebeck coefficients obtained experimentally and by calculation are apparent, suggesting other factors may need to be considered in the latter. Using a melt-anneal-sinter process, Li et al [62] prepared single-phase materials of $Cu_{1-x}Fe_{1+x}S_2$ over the compositional range ($0 \leq x \leq 0.1$), enabling the charge carrier concentration to be tuned over a wide range. Iron substitution leads to reductions in thermal conductivity, which

calculations suggest is due to the large strain-field fluctuations introduced by a disordered distribution of iron cations, leading to enhanced phonon scattering. This leads to a substantial increase in the figure-of-merit which reaches $(ZT)_{max}$ = 0.33 at 700 K for a sample of composition $Cu_{0.97}Fe_{1.03}S_2$.

Given the importance of the interaction of the charge carrier with the magnetic moment, substitution of a magnetic ion at the copper site has also been explored through preparation of the *n*-type materials $Cu_{1-x}M_xFeS_{2-y}$ (*M* = Mn, Co, Ni; $x \leq 0.5$; $y \leq 0.02$) [63,64] Large values of |S| (200 – 340 μV K^{-1}) are retained and maximum ZT values reach 0.20 at 623 K for 3% manganese substitution. More promisingly, given the constraints imposed by the relatively high thermal conductivity, substantial reductions in thermal conductivity are observed and a value of κ = 1.2 W m^{-1} K^{-1} is reached at 623 K at 5% manganese substitution. A TEM study of the best performing material $Cu_{0.95}Mn_{0.03}FeS_2$ reveals twinning and an inhomogenous distribution of the Mn substituent, which may contribute to the low measured thermal conductivity through local disorder. The analogous palladium-substituted materials, $Cu_{1-x}Pd_xFeS_2$, are single-phases for $x < 0.02$, with a PdS impurity appearing at higher levels of substitution.[65] This is present as a micro-precipitate within the $CuFeS_2$ matrix similar to the ZnS inclusions reported in $Cu_{1-x}Zn_xFeS_2$.[66] The formation of the secondary PdS phase, accompanied by Fe_{Cu} antisite defects, has an impact on the lattice thermal conductivity. Above the solubility limit ($x \approx 0.2$), phonon scattering from small PdS inclusions decreases κ_L, while at higher nominal substitution levels, defect scattering becomes the dominant contribution to κ_L. The electrical-transport properties show the expected behaviour (increased conductivity, decreased Seebeck coefficient) associated with an increase in carrier concentration on substitution, resulting in power factors that are almost temperature invariant and which show little compositional dependence at $x > 0.05$, with the result that ZT increases with palladium content, reaching ZT = 0.19 at 573 K for the composition x = 0.10.

Partial substitution of iron by the heavier indium cation offers scope to reduce the relatively high thermal conductivity of $CuFeS_2$ through mass fluctuation scattering. The non-magnetic nature of In^{3+} should also weaken magnetic scattering of charge carriers. The series $CuFe_{1-x}In_xS_2$ exhibits solid-solution behaviour over the range $0 \leq x \leq 0.08$.[67] At the solubility limit, the lattice contribution to the thermal conductivity is reduced by *ca.* 60 % at 300 K. Calculations indicate the effective mass is effectively invariant with composition suggesting that indium substitution can be effected with no significant change to band structure. Electrical conductivity falls with increasing indium content, while the compositional

dependence of the Seebeck coefficient is less systematics: initially falling slightly before showing higher values for x = 0.08. Together, these result in power factors that fall with increasing indium content. However, this reduction is compensated for by the appreciable reduction in thermal conductivity, leading to a figure-of-merit that is increased by 30 % from that of the parent phase, to $(ZT)_{max}$ = 0.17 at 630 K for x = 0.04. Although the range of iron incorporation in the isostructural $CuInS_2$ is slightly greater (x_{max} = 0.15), thermoelectric properties are significantly reduced from those of iron-rich phases.[68]

Sulfur deficiency has a beneficial impact on thermoelectric properties. Both electrical resistivity and thermal conductivity decrease with decreasing sulfur content, increasing ZT to 0.21 at 573 K in $CuFeS_{1.80}$.[69] However, as has been pointed out by Lefevre et al[63] this high level of sulfur deficiency corresponds to compositions where alternative structure types, such as talnakhite and mooihoekite that are difficult to distinguish from chalcopyrite by X-ray methods, may be stabilised. Combining sulfur deficiency with substitution at the copper site, results in a maximum ZT of 0.20 at 673 K in $Cu_{0.98}Co_{0.02}FeS_{1.98.}$[63] Transport properties are similar to those for analogous phases with the same charge carrier concentration in which there are no sulfur vacancies, consistent with the substituent being Co^{2+}. The partial replacement of sulfur with the heavier congener selenium, offers an alternative strategy to improve electrical properties through manipulation of the band structure, with the added possibility to reduce the thermal conductivity through mass-fluctuation scattering. Despite the different structure adopted by $CuFeSe_2$, solid solution behaviour is found in the series $CuFeS_{2-2x}Se_{2x}$ over a relatively wide compositional range ($0 \leq x < 0.25$),[70] with an impurity of FeSe appearing at x = 0.30. Selenium substitution principally affects the power factor, through reductions in electrical resistivity (by a factor of two at high temperatures), potentially due to band broadening effects, while the changes to the Seebeck coefficient are less pronounced. The peak power factor occurs near room temperature and is increased by almost a factor of two for x = 0.2. Although thermal conductivity at sub-ambient temperatures is reduced on selenium substitution, the impact at higher temperatures is marginal and $(ZT)_{max} \approx 0.15$ at 675 K.

In addition to the use of chemical substitution to adjust the carrier concentration and to lower the thermal conductivity, efforts to improve the thermoelectric properties of chalcopyrite have included novel synthesis methods to exploit nanostructuring. Nanocrystals of copper-iron sulfide have been synthesised by the solution-based polyol method for different Cu:Fe ratios.[71] The Seebeck coefficient is dependent on the Cu:Fe ratio of the initial reaction

mixture. Surprisingly the Seebeck coefficient of the nanoparticulate phases indicate *p*-type conduction, in contrast with the widely-observed *n*-type behaviour of the bulk phase. Similar *p*-type behaviour has been observed in nanocrystals grown by the hot-injection method.[72,73] Chalcopyrite has also been synthesised by an alternative approach in which pelletized mixtures of elemental powders are subjected to a short (< 90 s) heating period to induce ignition and hence rapid reaction.[74] The loss of sulfur during reaction necessitated the use of sulfur-rich mixtures and single-phase material with > 98% of crystallographic density resulted from a mixture of composition $CuFeS_{2.3}$ However the highest performance of $(ZT)_{max} = 0.23$ (at 625 K), slightly exceeding that of the best obtained in the conventionally-prepared bulk sample, $CuFeS_{1.8}$, was achieved in a metal-rich composition that exhibits two-phase behaviour. The two-phase nature of the product introduces characteristics of a nanocomposite and the resulting phase boundaries serve to scatter low frequency phonons, thereby reducing the thermal conductivity.

4.1.b Quaternary Cation-Ordered Phases Derived from Zinc Blende

While the majority of investigations of quaternary chalcogenides with the kesterite/stannite-type structure have focused on the selenides,[75,76,77,78] there has been a limited number of studies of the corresponding sulfides, which theoretical work suggests should exhibit both similar properties,[79] and response to doping, to the selenide analogues.[80] Despite a relatively large band gap, the *p*-type quaternary chalcogenides have attracted attention as candidate thermoelectrics owing to their intrinsically low thermal conductivity, coupled with the capacity to tune transport properties by chemical means. Single crystals of Cu_2ZnSnS_4 (CZTS) exhibit a thermal conductivity of $\kappa = 3$ W m^{-1} K^{-1} at 300 K, the low value being attributed to anti-site disorder on the Cu/Zn sub-lattices.[81] Changing the Cu:Zn ratio has a relatively minor impact on κ, whereas the effect on the electrical transport properties is more marked. At high temperatures both copper deficiency and excess copper increase the electrical conductivity, due to an increase in hole concentration through an increase in copper vacancies (Cu poor) or Cu_{Zn} anti-site defects (Cu rich). The former has the more marked effect on conductivity. This leads to an increase in power factor, despite the reduction in Seebeck coefficient that accompanies the increased electrical conductivity. This leads in the Cu-poor phase, to a maximum ZT = 0.2 at 400 K: the limit of the measurements. This greatly exceeds the performance of SPS-processed nanocrystals of CZTS at the same temperature ($ZT \approx 0.03$).[82] Copper doping, through partial replacement of zinc with copper[83] results in a marked increase in electrical conductivity and decrease in Seebeck coefficient, due to the

creation of holes associated with (formally) Cu^{2+}. The power factor of the copper-rich phase $Cu_{2.1}Zn_{0.9}SnS_4$ is increased, which coupled with the retention of a low thermal conductivity, raises ZT to 0.36 at 700 K.

The electrical resistivity of the germanium analogue Cu_2ZnGeS_4 (CZGS) prepared by solid-state reaction, is considerably higher than that of CZTS.[84] Progressive substitution of sulfur with the more covalent selenium reduces the band effective mass and increases carrier mobility, leading to a fall in resistivity. Thermal conductivity of the mixed-anion phases is lower than that of either end-member phase and passes through a minimum at a 50:50 S:Se ratio. This may be attributed to anion disorder which results in mass fluctuation scattering and strain contrast, both of which serve to scatter phonons. Anion substitution also has an impact on band structure,[85] altering the relative energies of the VBM and CBM and leading to a decrease in E_g, as is observed experimentally. [86]

Although the electrical-transport properties make the mixed-anion phases unattractive for thermoelectric applications, suitable chemical substitution may be used to increase the charge carrier density. This approach was adopted[87] in single crystalline $Cu_{2-y}ZnSn(S_{1-x}Se_x)_4$, where *ca.* 10 % copper deficiency increases the electrical conductivity through the formation of shallow Cu acceptor levels. The figure-of-merit increases with selenium content, reaching ZT = 0.32 at 400 K for the pure selenide. In contrast with the mixed-anion CZGSSe phases[84] discussed above, thermal conductivity decreases progressively as sulfur is replaced by the heavier element, selenium, with no minimum value at intermediate compositions being observed. This difference in behaviour may be associated with the copper-deficient nature of the materials, which leads to a higher charge-carrier contribution to the thermal conductivity. Nanocrystalline mixed anion phases, CZTSSe, synthesized solvothermally[86] show thermal conductivities that are reduced from those of their bulk counterparts, all lying below 1 W m^{-1} K^{-1}. This may be associated with increased grain boundary scattering of phonons, given that the nanocrystals are of the order of 5 - 7 nm, although it is unclear if porosity plays a role, given that densities are not reported. E_g decreases linearly with increasing selenium content but the variation in electrical-transport properties is less systematic. The highest figure-of-merit (ZT = 0.48 at 700 K) occurs for 25 % selenium substitution.

The stannite-phase Cu_2FeSnS_4 and a copper-rich stannite-type phase, kuramite (Cu_3SnS_4), form a solid solution[88] $Cu_{2+x}Fe_{1-x}SnS_{4-\delta}$ over the range ($0 << x < 1$). Phases are anion deficient ($\delta \leq 0.4$), while above $x = 0.6$, the tetragonal distortion is effectively removed ($c/2a = 1.0$). Compositions with $x > 0.8$ show a metallic $\rho(T)$ dependence with Seebeck coefficient, $S \approx$

100 μV K^{-1}, suggesting they are degenerate *p*-type semiconductors. While the figure-of-merit is increased relative to the stannite end-member, it reaches only ZT ≈ 0.04 at 300 K, the limit of the measurement range, principally due to the modest Seebeck coefficient and increased thermal conductivity (κ ≈ 1.5 W m^{-1} K^{-1}).

4. 2. Binary Copper Sulfides and their Derivatives

Following the report of high thermoelectric performance in Cu_2Se,[21] attention has focused on the corresponding sulfide[89] as a less toxic alternative, given the structural similarities of the two high-temperature phases. While stoichiometric Cu_2S is an intrinsic semiconductor, copper deficiency leads to *p*-type behaviour, with the hole concentration increasing markedly with the number of vacancies.[90] This leads to an increased electrical conductivity and decreased Seebeck coefficient. However, the thermal conductivity is less affected by the copper content and low values (< 0.6 W m^{-1} K^{-1}) are observed for compositions in the range $0 \leq x \leq 0.02$. The temperature-induced phase transitions outlined in Section 3 manifest themselves in anomalies in the temperature-dependence of the electrical and thermal transport properties, leading to the identification of three regions. In the high temperature regime, thermal conductivity shows a weak temperature dependence which is taken as evidence of a highly disordered liquid-like copper sub-lattice (Figure 7), indicating the PLEC concept, successfully exploited in copper selenide, is transferable to the sulfide. First principles calculations[91] of the electronic structure and electrical transport properties of $Cu_{2-x}S$, both with (x=0.02) and without (x=0) vacancies in the low- and high-temperature phases confirm this. They reveal that structural variations associated with the copper sites have relatively little impact on the electronic states at the band edge and consequently electrical-transport properties. In the low temperature phase, instead of introducing impurity states in the VB-CB gap, the creation of vacancies lowers the Fermi level into the VB. Similarly the VBM in the high-temperature structure is not affected significantly by vacancy formation or disorder. This supports the view that the material behaves as an electron-crystal, in which the electrical properties are determined principally by the anion sub-lattice and copper vacancies serve as a source of holes. Remarkably the highest thermoelectric performance for $Cu_{2-x}S$ (ZT = 1.7 at 1000 K for $Cu_{1.97}S$)[90] exceeds that of the best performing selenide (ZT = 1.5 at 1000 K).[21] This can be traced to an exceptionally low lattice thermal conductivity (κ_L) in the sulfide, despite the lighter mass of the anion. This is associated with the softness of the shear

modes in $Cu_{2-x}S$ that reduces the transverse phonon velocity and the average speed of sound in the liquid-like state.[90] Indeed the calculated minimum value of κ_L is below the minimum thermal conductivity determined from the Cahill formula,[92] suggesting that only a fraction of the modes contribute to heat propagation.

X-ray photoelectron spectroscopy of $Cu_{2-x}S$ over the range of compositions ($0.04 \leq x \leq 0.20$)[43] demonstrates that the copper valence state is insensitive to copper content, whereas the thermoelectric properties are dependent on both copper content and the nature of the sulfur close packing. The ZT(x) dependence shows a peak around x = 0.04, reaching a value of ZT = 0.8 at 750 K. When this is compared with the theoretical work presented in Figure 3 of the paper by He et al.,[90] it suggests the carrier concentration is not fully optimised.

The mode of preparation and fabrication of $Cu_{2-x}S$ phases also plays a key role in determining thermoelectric performance. In part this can be traced to the volatilization of sulfur at higher temperatures, which can lead to compositional changes during consolidation by hot pressing or spark plasma sintering (SPS). On occasion, this may be beneficial as it can introduce nanoprecipitates of a second phase that serves to reduce thermal conductivity, as discussed below for the partial decomposition of $Cu_{1.8}S$ to $Cu_{1.96}S$ due to sulfur loss during SPS, although it may introduce issues of long-term stability during operation at elevated temperatures. In an effort to avoid compositional changes during consolidation, Zhao et al,[93] prepared dense void-free monoliths of $Cu_{2-x}S$ (x = 0.0, 0.03) suitable for electrical and thermal transport measurements directly from the melt, obviating the need for a consolidation step. While exceptionally low thermal conductivities ($0.3 \leq \kappa/W\ m^{-1}\ K^{-1} \leq 0.5$) are observed for both compositions, the superior electrical properties of the defective phase, results in quite different figures-of-merit: that of $Cu_{1.97}S$ reaching the remarkable value of ZT = 1.9 at 973 K. However, repeated measurements of thermoelectric properties reveal that the electrical transport properties show poor reproducibility, which may be a consequence of copper-ion migration or sulfur volatilization on repeated heating-cooling cycles. Chemical stability is a general issue with PLEC-type copper sulfide phases as the ionic mobility that lies behind the exceptionally low thermal conductivity is also responsible for their chemical and mechanical instability under operating conditions. In the case of Cu_2S, it has been shown[94] that at elevated temperatures and current flow of a few Amperes, copper ions migrate to the negative end of the thermoelement, appearing as copper whiskers. This is accompanied by the appearance of cracks due to the compositional change of the bulk. In the same study, digenite ($Cu_{1.8}S$) was

identified as a potentially more promising material for applications as no degradation under an electric field was observed, even at high current densities.

Although the Seebeck coefficient of $Cu_{1.8}S$ is relatively low (*ca*. 10 μV K^{-1}), a band gap of E_g ≈ 1.5 eV and a high electrical conductivity suggest it is a suitable candidate for optimization of the thermoelectric properties. Using mechanochemical synthesis of $Cu_{1.8}S$ followed by consolidation by spark plasma sintering (SPS), Ge et al,[95] succeeded in producing a material, which exhibits a maximum figure-of-merit, ZT = 0.5 at 673 K. The higher than expected performance is principally attributable to a reduction in thermal conductivity of a sample consolidated at 973 K, over those sintered at lower temperature. This appears to be associated with partial decomposition through sulfur volatilization at the higher sintering temperature. In addition to generating precipitates of a Cu-rich phase ($Cu_{1.96}S$), sulfur loss generates pores, with sizes in the range 100 – 500 nm that impede heat flow.

Doping $Cu_{1.8}S$ with sodium[96] produces marked improvements in thermoelectric properties by effecting reductions in carrier concentration, thereby enhancing the Seebeck coefficient. This, together with the creation of nanopores and nanograins, which reduce thermal conductivity, increases the figure-of-merit to 1.1 at 773 K in $Na_{0.01}Cu_{1.8}S$, due to the combination of a high electrical conductivity and low thermal conductivity. Surprisingly, the total thermal conductivity is lower than that for the charge carrier component (κ_e) determined using the measured electrical conductivity and the Wiedemann-Franz Law. This appears to question the applicability of this expression to materials that exhibit a liquid-like state, where there is an ionic contribution to electrical and thermal transport. Concerns have also been expressed about the reliability of laser-flash measurements of thermal conductivity in materials undergoing phase transitions, analogous to those in copper sulfides.[97]

More modest enhancements in performance have been achieved through doping with titanium ($(ZT)_{max}$ = 0.54 at 673 K)[98] and with bismuth ($(ZT)_{max}$ = 0.61 at 673 K)[99]. In the former case, higher levels of titanium doping induce sulfur volatilization and the formation of Cu_4TiS_4 and $Cu_{1.96}S$ as secondary phases, which may be responsible for the significant reduction in thermal conductivity observed. Bismuth doping also leads to sulfur volatilization, which at higher doping levels results in the formation of Cu_3CuS_3 and $Cu_{1.96}S$. The enhanced figure-of-merit achieved at low doping levels (*ca.* 1%) is primarily associated with improvements in electrical conductivity, while maintaining the Seebeck coefficient close to that of the pristine phase.

Improvements to the thermoelectric properties of digenite result on mechanical alloying with small (< 3 wt. %) amounts of PbS.[100] Below the solubility limit of *ca*. 2 wt. %, lead ions are accommodated at interstitial sites and suppress the sulfur volatilization that affects carrier concentration, generally observed when heteroatoms are introduced into $Cu_{1.8}S$. Although measurements were conducted over a more limited temperature range of $323 \leq T/K \leq 773$, the results show that the electrical transport properties are largely retained in Pb-doped phases in this temperature region. This is attributed to the control over hole carrier concentration, which falls by < 14% over the entire solid-solution range, due to the suppression of sulfur volatilization and the narrowing of the band gap on introduction of PbS. Moreover, the introduction of lead also reduces the thermal conductivity through the introduction of point defects and interfaces, more than doubling the figure-of-merit for $Cu_{1.8}S$ containing 2 wt.% PbS to ZT = 1.1 at 773 K. A fast doping strategy in which In_2S_3 is manually ground with a ball-milled sample and the mixture consolidated by SPS using a short sintering time of 5 min.[101] yields a material with ZT = 1.4 at 773 K for 3 wt.% In_2S_3 incorporation. However, powder X-ray diffraction data indicate this is significantly above the solubility limit and the material should perhaps be better considered as a composite. Electron microscopy indicates the second phase is located within nanopores within the composite, providing an effective means of scattering phonons and lowering thermal conductivity.

Efforts have also been made to exploit nanocompositing in $Cu_{1.8}S$, through introduction of a second phase: an approach that has been applied successfully to many tellurides. Dispersal of nanoparticles of WSe_2 in $Cu_{1.8}S$[102] is accompanied by sulfur volatilization, reducing the electrical conductivity, particularly at low temperature and enhancing the Seebeck coefficient. While the power factor is increased slightly on nanocompositing, a 50% reduction in thermal conductivity contributes to a maximum figure-of-merit reaching ZT = 1.22 with 1 wt.% of WSe_2. A similar approach has been adopted using graphene as a nanocompositing agent,[103] leading to a higher maximum ZT=1.56 at 873 K. Interestingly, in relation to the problems of decomposition outlined above, the composites show good reproducibility in electrical properties on repeated cycling. This approach has been extended to nanocompositing of $Cu_{1.8}S$ with both Bi_2S_3 and Bi_2S_3@Bi core-shell nanorods[104]

4.3. Thermoelectric Sulfides Derived from Copper-Containing Minerals

4.3.a Bornite and Chemically-modified Derivatives

One approach to overcoming the problems of stability associated with antifluorite-type copper sulfides that exhibit PLEC-type behaviour, is the introduction of a second cation to suppress copper-ion migration. As described above, bornite shows parallels with the binary copper sulfides, not least in the adoption of a cation-deficient antifluorite structure at high temperatures, that undergoes a sequence of ordering transitions on cooling. Mössbauer and magnetic data indicate the assignment of formal oxidation states as $Cu^{+}_{5}Fe^{3+}S_4$,[105] making the stoichiometric phase a semiconductor. More recent Mössbauer measurements[106] indicate a partial electron transfer from copper to iron cations; the oxidation state of the latter decreasing to $Fe^{(3-x)+}$. Synthetic bornite shows an exceptionally low thermal conductivity of < 0.5 W $m^{-1}K^{-1}$ over a wide temperature range.[107] The ball-milled stoichiometric material has a higher ZT= 0.55 at 543 K[108] compared with that produced by conventional high-temperature processing.[107] At elevated temperatures formation of a solid solution, $m Cu_8S_4 \cdot (1-m) Cu_5FeS_4$ with antifluorite-type Cu_2S, results in a maximum figure-of-merit ZT = 1.2 at 900 K for m = 0.8.[107]

These observations motivated efforts to use chemical manipulation to improve the thermoelectric properties of bornite through preparation of non-stoichiometric series,[109] $Cu_{5-x}FeS_4$ and $Cu_{5+y}Fe_{1-y}S_4$ in which both the carrier concentration and vacancy levels were controlled. Single-phase materials exist over the fairly limited compositional ranges $x \leq 0.1$ and $y \leq 0.08$ respectively. Introduction of copper vacancies as x is increased, decreases the resistivity through the creation of holes associated with formally Cu^{2+}, whereas adjusting the Cu:Fe ratio by varying y, achieves a similar result, albeit with retention of full cation-site occupancy. The figure-of-merit is increased through both of these methods, reaching ZT ≈ 0.6 at 550 K. A combination of these two approaches, through preparation of $Cu_{4.94+z}Fe_{1-z}S_4$ ($z \leq 0.04$), leads to further improvements in thermoelectric performance, with $(ZT)_{max}$ reaching 0.79 at 550 K, amongst the highest values for a sulfide at this temperature. Remarkably, the power factors of all three non-stoichiometric series scale almost linearly with the formal Cu^{2+} contents, suggesting the creation of holes plays the dominant role in determining the thermoelectric properties. However, the highest figures-of-merit also require the presence of cation vacancies, which reduce the thermal conductivity. While the thermal conductivity of phases which retain full occupancy of cation sites increases progressively with Cu(II) content, due to the increased charge carrier contribution, that in materials in which there are vacancies shows a weaker compositional dependence. The maximum ZT requires Cu(II) contents of 2 - 2.8 % with *ca*. 1 % of vacancies simultaneously present.

Significantly from the perspective of device applications, the presence of iron on tetrahedral sites appears to suppress degradation and properties are retained on cycling.

Substitution of low levels of manganese for iron in the orthorhombic phase leads to an increase in resistivity and Seebeck coefficient in $Cu_5Fe_{1-x}Mn_xS_4$,[108] despite the increase in hole content when Fe(III) is replaced by Mn(II), while at $x > 0.03$, both S and ρ decrease. Thermal conductivity shows a relatively weak dependence on manganese content, which together with power factors that are almost compositionally invariant, due to the self-compensating nature of changes to S and ρ, leads to a figure-of-merit comparable with that of the un-substituted phase. The physical properties show anomalies in their temperature dependence at each of the structural phase transitions. The partial substitution of sulfur by selenium[110] in $Cu_5FeS_{4-x}Se_x$ ($0 \leq x \leq 0.6$) stabilises the intermediate cubic 2a structure over the fully vacancy-ordered, orthorhombic 4a structure, at temperatures up to 475 K. This appears to be related to the high quenching rate of the SPS consolidation method employed. The suppression of the 2a $\rightarrow$ 4a transition may offer advantages from the perspective of device operation. Above 475 K, the 2a structure co-exists with the high-temperature disordered antifluorite structure; some decomposition to chalcopyrite-type phases is observed above 540 K. Selenium substitution also increases the metallic character, evidenced by higher carrier mobilities, leading to marked reductions in resistivity. This reaches *ca*. 4 mΩ cm at $x = 0.6$, with substituted phases showing a weak $\rho(T)$ dependence. Although substitution also decreases the Seebeck coefficient, reductions are less marked and the power factor is increased, reaching *ca*. 0.5 mW m^{-1} K^{-2} at 540 K for $x = 0.4$. Furthermore the lattice thermal conductivity is reduced significantly, primarily as the result of mass-fluctuation scattering, leading to $(ZT)_{max} \approx 0.5$ at 540 K for compositions in the range $0.2 \leq x \leq 0.4$.

$Cu_{5-x}Co_xFeS_4$ offers a rare example of copper substitution in bornite.[111] The orthorhombic 4a structure is found throughout the compositional range $0 \leq x \leq 0.08$ following hot pressing of mechanochemically alloyed samples. Substitution reduces the hole concentration and increases both the resistivity and Seebeck coefficient, while power factors increase by 20 % to *ca*. 0.3 mW m^{-1} K^{-2} at 590 K ($x = 0.04$). At low levels of substitution ($0.02 \leq x < 0.04$), the thermal conductivity is reduced by *ca*. 30% at room temperature and reaches a remarkably low value of 0.22 W m^{-1} K^{-1} for $Cu_{5.96}Co_{0.04}FeS_4$ at 473 K. Whilst the retention of nano-sized grains (< 50 nm) on consolidation play a role in effecting reductions in thermal conductivity, the relatively low density of the consolidated materials undoubtedly has an impact. A

similarly low thermal conductivity is achieved in the analogous zinc-substituted phases, $Cu_{5-x}Zn_xFeS_4$, above a critical level of substitution, $x_c > 0.04$.[112] Both resistivity and Seebeck coefficient are also increased for $x > 0.04$ but in contrast with cobalt substitution, there is relatively little change in power factor compared with that of the parent phase. Double substitution at the two cation sites, $Cu_{4.96}Co_{0.04}Fe_{1-x}Zn_xS_4$ ($0 \leq x \leq 0.06$) leads to an improvement in power factor, which when combined with the low thermal conductivity, typical of the substituted phases, increases $(ZT)_{max}$ to 0.6 at 590 K ($x = 0.04$). Micro-hardness generally increases with the level of substitution, suggesting the non-stoichiometric phases have superior mechanical properties, which may offer advantages in device construction and stability.

Although the majority of bornite-type phases have been synthesised by high-temperature processing or by high-energy ball milling, solution-based routes have been explored in an effort to generate nanoparticulate forms. Colloidal synthesis using hot-injection of a sulfur source into a solution of the two cations has been used to prepare nanocrystals of Cu_5FeS_4[113] at a range of temperatures. On consolidation by SPS the orthorhombic 4a phase is formed. Although grain growth occurs on sintering, some nanoparticles are retained. Transport properties are significantly different from those of materials prepared by conventional means. This may be traced to marked deviations from nominal stoichiometry: chemical analysis revealing that the products are copper-rich and iron-deficient. The greatly increased charge-carrier density that results, increases the electrical conductivity, leading to ZT = 0.56 at 700 K, an increase of 40 - 47 % over values reported for nominally stoichiometric material prepared by conventional means[107,109] and comparable to that reported by Guelou et al.[108] albeit at the lower temperature of 543 K. Colloidal processing has also been used to produce icosahedral nanoparticles,[114] containing a high density of twin boundaries to enhance phonon scattering. The nanoparticles have a core-shell structure, in which an iron-rich orthorhombic (4a) core is encapsulated in a copper-rich, iron-deficient cubic (a) phase. The more conductive iron-deficient phase, increases the electrical conductivity and leads to a higher power factor. Despite the higher charge-carrier contribution, κ_e, thermal conductivity remains low, resulting in $(ZT)_{max} = 0.62$ at 710 K, amongst the highest for what is nominally stoichiometric bornite.

An interesting alternative approach to the synthesis of nanostructured bornite is the use of nanoparticles of Cu_2S and FeS as building blocks.[115] Blending of dispersions of the

nanoparticulate binary sulfides followed by consolidation by SPS results in a material that is predominantly bornite, for Cu_2S:FeS volume ratios of 9:1 and 3:1. The principal impurity is nukundamite, $(Cu,Fe)_4S_4$, in each case. Thermal conductivity is little affected by nanostructuring or the presence of an impurity phase, the low values of the conventionally-prepared material being retained. However, the electrical properties are enhanced, which increases ZT to 0.55 at 663 K; a value comparable with the highest values achieved by materials produced using a colloidal method[113] or by ball milling.[108]

4.3.b Colusite-Related Materials

The potential of colusite-related materials as Earth-abundant *p*-type thermoelectrics was first recognized by Suekuni *et al.*[116] who observed a high power factor in $Cu_{26}V_2B_6S_{32}$ (*B* = Ge, Sn). This, together with an exceptionally low lattice thermal conductivity leads to ZT = 0.73 at 663 K in the germanium-containing phase. Band structure calculations on colusites[117] reveal that the Fermi level penetrates into the VB manifold, consistent with the observed p-type behaviour. Electronic states near the top of the VB arise from admixture of 3*p* orbitals of S (at the 24*i* site) and copper 3*d* orbitals, whereas the minimum in the conduction band is composed of vanadium and S (8*e* site) orbitals. The complexity of the colusite structure contributes to a remarkably low thermal conductivity of *ca*. 0.5 W m^{-1} K^{-1}. The large number of atoms of 64 - 66 per primitive unit cell (*N*), lowers the group velocity of the optical modes and reduces the efficiency of heat transport by acoustic modes, which varies as $1/N$ if boundary scattering dominates (or $1/N^{1/3}$ if Umklapp scattering is dominant).[118] The V-S bonds are also strong and ionic, leading to weakening of the Cu-S bonds: a feature which, together with the calculated compression of the acoustic branches, may contribute to the low thermal conductivity through low-frequency optic modes. Magnetic susceptibility data for the vanadium-containing material show a weak temperature dependence,[119] suggesting formal oxidation states of Cu^+, V^{5+} and B^{4+} (*B* = Ge, Sn). However, this creates a charge imbalance, indicating that the compounds are electron deficient, and may be formulated as $Cu_{22}^{+}Cu_4^{2+}A_2^{5+}B_6^{4+}S_{32}$ (*A* = V, Nb, Ta; *B* = Ge, Sn), although the non-magnetic character and metallic ρ(T) behaviour indicates that the holes are not localised, as this formalism implies.

Stoichiometric $Cu_{26}V_2B_6S_{32}$ synthesised by conventional high-temperature methods is essentially monophasic, when *B* = Ge but for the tin congener, two colusite phases of slightly different compositions can be identified by X-ray diffraction.[116,119] Both tin and germanium analogues are copper deficient, with the vacancies created being occupied by excess

vanadium/tin cations. Two-phase behaviour persists in copper-deficient phases, $Cu_{26-x}V_2Sn_6S_{32}$,[120] although surprisingly the resistivity is increased, despite an increase in carrier density. Partial replacement of copper by zinc in $Cu_{26-x}Zn_xV_2B_6S_{32}$ has been used[119,121] to tune the hole carrier-concentration by introducing electrons, in an effort to improve on the relatively poor Seebeck coefficient of $Cu_{26}V_2B_6S_{32}$. Substitution suppresses the phase separation and increases both the electrical resistivity and thermopower significantly. While *p*-type metallic behaviour is retained for $x < 4$, the change to 3D Variable Range Hopping conduction at $x = 4$, suggests the introduction of electrons displaces the Fermi level to localized states near the top of the valence band. Substitution increases both resistivity and Seebeck coefficient. The electronic term dominates the thermal conductivity, which is around 3 W m^{-1} K^{-1} at 300 K: the highest temperature for which measurements were made. Powder neutron diffraction data for mechanically alloyed $Cu_{26-x}Zn_xV_2Sn_6S_{32}$,[121] confirms that zinc substitutes for copper in the tetrahedral sites, while electron microscopy and X-ray diffraction provide further evidence for the phase separation of the un-substituted phase previously noted by Suekuni *et al.*[116] The decrease in hole concentration through the electron doping provided by zinc, leads to an almost linear increase in S_{300K} between $x = 0$ and $x= 2$. S(T) is linear throughout the extended temperature range $300 < T/K \leq 700$[121], which together with the metal-like $\rho(T)$ suggests metallic behaviour is retained at these levels of doping. The power factor reaches its maximum value at $x = 1$. Thermal conductivity shows a weak compositional dependence in the range $0 \leq x \leq 1$, but is reduced by 25 - 30% for $x = 2$. The figure-of-merit reaches a maximum $ZT = 0.4$ at 700 K for $x = 1$ and 2.

A surprising degree of complexity in the relationship between composition, structure and thermoelectric properties in colusite-type phases is beginning to emerge, exemplified by the discrepancies in the values of the Seebeck coefficient and thermal conductivity reported in different studies. Measured properties fall into two principal classes. Apparently stoichiometric phases with low Seebeck coefficients ($S \approx 30$ μV K^{-1}), indicative of more metallic behaviour, exhibit lattice thermal conductivities in the range $0.90 \leq \kappa_L/W\ m^{-1}\ K^{-1} \leq 1.4$,[119,121] near room temperature, whereas lower values (*ca.* 0.5 W m^{-1} K^{-1}) occur in materials with higher resistivities and Seebeck coefficients ($S \geq 100$ μV K^{-1}).[116,122] This strongly suggests that the properties of colusite-type phases prepared in the laboratory are sensitive to the mode of preparation and consolidation. Recent work[117] supports this conclusion. Mechanochemically-prepared materials of nominal composition $Cu_{26}V_2Sn_6S_{32}$ consolidated by SPS at 873 K and by hot pressing at 1073 K show marked differences in composition,

microstructure and transport properties. The material resulting from consolidation at 973 K appears to be well crystallised and ordered. By contrast, consolidation at the higher temperature leads to a cation-disordered, copper-rich, sulfur-poor phase, due to volatilization of sulfur. This leads to 1-D line defects involving substitution of tin with vanadium and/or copper. In addition, coherent intergrowths of a disordered phase are evident in the material sintered at 1073 K, analogous to those observed in the natural mineral.[123] The electrical transport properties of $Cu_{26}V_2Sn_6S_{32}$ consolidated under different conditions are consistent with the two types of behaviour reported previously. High-temperature sintering produces a material with a much higher resistivity and Seebeck coefficient than when sintering is carried out at 873 K. The sulfur loss that occurs at 1073 K reduces the hole carrier density by almost 60%, while the resulting disorder reduces the carrier mobility by a factor of two compared to the values obtained when sintering is carried out at 873 K. The phase sintered at low temperature, however, has a much higher thermal conductivity (κ = 2.19 to 2.9 W m^{-1} K^{-1}) than that resulting from high-temperature processing, due to larger carrier concentration and the absence of structural defects. Point defects in the hot-pressed material scatter short wavelength phonons, while the intergrowth regions contribute to the scattering of those with medium wavelength. Together, these reduce the thermal conductivity to $\kappa \approx 0.66$ W m^{-1} K^{-2}. This results in a maximum ZT = 0.93 at 675 K, almost a factor of three greater than that obtained by sintering at 873 K, demonstrating the importance of controlling the defective nature of these phases through careful regulation of processing conditions. In the case of $Cu_{26-x}Nb_2Sn_{6+x}S_{32}$ ($-0.3 \leq x \leq 1.2$), exsolution into ordered and disordered regions has been shown to depend critically on the Cu/Sn ratio;[124] the fraction of the ordered domain, increasing with decreasing x. However, the sintering temperature plays a key role, sulfur loss leading to the introduction of interstitial cations when the ordered structure is hot pressed at 973 K, resulting in reduced lattice thermal conductivity.

The partial replacement of copper by transition-series cations, other than zinc, has been explored.[125,] In common with other colusite-related phases, $Cu_{24}M_2V_2Ge_6S_{32}$ (M = Co, Ni) materials exhibit low lattice thermal conductivities, which may be influenced by the minor impurity phases apparent in powder X-ray diffraction data. Cobalt-substitution increases both resistivity and Seebeck coefficient, consistent with expectations for electron donation, whereas the reverse effect is apparent in the nickel-containing phase, which exhibits a more metallic ρ(T) behaviour. Despite the low thermal conductivities, the electrical properties limit the figures-of-merit to a maximum ZT = 0.5 at 690 K, obtained in $Cu_{24}Ni_2V_2Ge_6S_{32}$.

The initial work on vanadium-containing phases has been extended to the group 5 analogues, Nb and Ta. Materials $Cu_{26}A_2Sn_6S_{32}$ (*A* = Nb, Ta),[122] as-prepared from the melt, show similar two-phase behaviour to that of the vanadium congener. Hot pressing causes phase coalescence, although binary copper sulfide impurities can be identified when *A* = Ta, leading this phase to exhibit a slightly lower lattice thermal conductivity (κ_L) and a reduced electrical resistivity (ρ). The high Seebeck coefficient leads to power factors in the range 0.6 – 0.7 W m^{-1} K^{-2} at moderate temperatures. However, when coupled with a low κ_L and ρ, this leads to the maximum figure-of-merit $(ZT)_{max}$ = 0.8 at 670 K for the tantalum-containing phase.

A complementary approach to exploiting the intrinsically low thermal conductivity of colusite phases, by tuning the electrical properties, is through *B*-cation non-stoichiometry. Bouyrie et al [126] have investigated materials, $Cu_{26}A_2B_{6-x}S_{32}$ (*A* = Nb, Ta; *B* = Ge, Sn; x = 0.0, 0.5). The as-prepared materials contain minor impurities, which largely disappear on sintering, although the unit-cell expansion suggests this may be accompanied by sulfur loss, as has been reported by other workers.[122] The Ta- and Nb-containing materials differ in the presence of micro-scale precipitates, principally of binary copper sulfides, in the former. As the micro-precipitates are larger than the mean-free path of the charge carriers, they have little impact on electrical transport. However, they serve to reduce the lattice contribution to thermal conductivity, with κ_L being reduced by *ca.* 20% in $Cu_{26}Ta_2Sn_{5.5}S_{32}$ from the already low value of κ_L = 0.44 W m^{-1} K^{-1} in the niobium analogue. The impact on electrical-transport properties appears to be more marked in the niobium-containing phases, which show a slight reduction in resistivity with *B*-site non-stoichiometry, leading to improvements in power factor. The changes in electrical and thermal conductivity, result in a maximum figure-of-merit that approaches unity in $Cu_{26}Ta_2Sn_{5.5}S_{32}$. However, the direct impact of *B*-site non-stoichiometry is obscured a little by the results of chemical analysis, which shows significant deviations from nominal compositions. Materials generally have an excess of copper (up to 30 Cu per formula unit) and, in some cases, a slight germanium excess, suggesting that the overall composition, albeit itself influenced by *B*-site non-stoichiometry, may play a significant role in determining the thermoelectric properties. It has been suggested[122] that additional copper cations occupy voids corresponding to 6*b* interstitial sites in the colusite structure. This led Bouyrie et al[127] to introduce cations with smaller radii than copper into the colusite structure through preparation of $Cu_{26}Nb_2Ge_6T_xS_{32}$ (where *T* = Co, Ni, Fe). However, in samples prepared by hot-pressing of melt-synthesised phases, the transition-series cations instead partially substitute Cu, Nb and Ge cations, evidenced by the small change in lattice

parameter. The resulting exsolution of Cu, Nb and Ge leads to compositional inhomogeneities, in the form of microscale precipitates. In contrast with the behaviour of the *B*-cation deficient phases described above, these precipitates have little impact on thermal conductivity, which retains a value ($\kappa \approx 0.4$ W m^{-1} K^{-1}) characteristic of colusites, at all temperatures. However, while iron substitution decreases both carrier concentration and mobility, impacting negatively on the power factor, a high power factor is retained on substitution with cobalt and nickel, leading to ZT ≈ 0.7 at 665 K, for the nominal compositions $Cu_{26}Nb_2Ge_6Ni_{0.5}S_{32}$ and $Cu_{26}Nb_2Ge_6Co_{0.5}S_{32}$, comparable with the performance of the unsubstituted phase.

4.3.c Tetrahedrite-Derived Phases

According to the formulation, $Cu_{12}Sb_4S_{13}$, stoichiometric tetrahedrite, possesses two holes per formula unit; a picture confirmed by band structure calculations. [128] This is consistent with magnetic susceptibility data which exhibit a weak temperature-dependent paramagnetism above 85 K,[129] indicative of delocalisation of the holes and accounting for the *p*-type metallic behaviour[130] observed above this temperature. The stoichiometric phase exhibits a low thermal conductivity (*ca*. 1 W m^{-1} K^{-1} at 300 K). However, the high charge-carrier concentration reduces the Seebeck coefficient, resulting in a modest power factor. Therefore considerable effort has been directed towards improving the power factor through partial substitution at the copper site to reduce the hole concentration. Materials of general formula $Cu_{12-x}M_xSb_4S_{13}$ ($0 \leq x \leq 2$) have been prepared for a wide range of substituents, *M*, that includes the transition-series cations Cr, Mn, Fe, Co, Ni, Cu, Zn and Cd[131,132,133,134,135,136,137,138,139] the group 14 elements Ge, Sn and Pb,[140,141,142] and the group 2 element, Mg.[143] X-ray photoelectron spectroscopy suggests that the transition-metal cations, Mn, Co, Ni, and Zn substitute in the +2 oxidation state while iron substitutes as Fe^{3+}.[128] Introduction of spin-polarized states through substitution with a transition-series cation also alters the band degeneracy in the vicinity of the Fermi level. Substitution of copper results in the addition of electrons to the top of the valence band raising the Fermi level towards the band gap. For a divalent (M^{2+}) substituent such as Zn^{2+}, the composition $Cu_{10}M_2Sb_4S_{13}$ places the Fermi level in the band gap, resulting in low electrical conductivity. Consequently the optimum properties are observed at significantly lower levels of substitution (Table 2). Substituents from group 14 have been shown to be present in the tetravalent state,[141]

effectively adding three electrons each to the valence band, with the result that the optimum doping level of 0.9 to 1.5 electrons per formula unit is achieved at lower levels of substitution.[142] Double substitution of copper by nickel and zinc appears to be particularly effective in enhancing thermoelectric performance, with values of ZT in excess of unity being achieved in $Cu_{10.5}Ni_{1.5}$ $Zn_{0.5}Sb_4S_{13}$ at the comparatively modest temperature of 723 K.[144,] In addition to raising the Fermi level, as is achieved by substitution with a single cation, Ni/Zn co-doping reduces both the electronic and lattice contributions to thermal conductivity. Furthermore, an additional valence band arising from Ni states split by spin polarization is introduced. The minority spin states located above the Fermi level are partially empty and serve as acceptor levels, thereby creating additional holes in the VB, the number of which increases with nickel content. This avoids the low electrical conductivity that results from complete filling of the valence band of $Cu_{12}Sb_4S_{14}$ when the non-magnetic ion, Zn, replaces two Cu atoms.

Substitution of the main-group cation, antimony, has also been explored, both in isolation, in phases $Cu_{12}Sb_{4-x}M_xS_{13}$ ($0.5 \leq x \leq 2.0$; M = Te[145,146], Bi[147]) and in conjunction with co-doping at the copper site.[148,149] Replacement of antimony by tellurium has a similar effect to that resulting from partial replacement of copper by a transition-series or post-transition-series element in raising the Fermi level, through addition of electrons to the top of the valence band. This reduces the carrier concentration, thereby enhancing the Seebeck coefficient, whilst also reducing the charge-carrier contribution to thermal conductivity, with optimum properties requiring < 3.5 at.% of Te. Similar behaviour is observed when bismuth is introduced at the antimony site.[147] Co-doping tellurium-substituted phases through simultaneous substitution of copper, does not lead to any significant improvement in performance over that achievable through substitution at either site individually.

Partial replacement of S with Se in $Cu_{12}Sb_4S_{13-x}Se_x$[150,151] and its zinc-substituted analogue $Cu_{11}ZnSb_4S_{13-x}Se_x$[152] ($0 \leq x \leq 2$) has been used to tune the band structure. Measurements over the temperature range $3 \leq T/K \leq 300$ reveal a significant drop in resistivity with Se substitution, whilst the Seebeck coefficient is largely unaffected. This has been attributed to an increase in the band degeneracy in the region of the Fermi level through displacement to higher energies of valence band levels with low effective masses. The 60% increase in power factor at 300 K, coupled with reductions in thermal conductivity due to alloy scattering leads

at x = 1, to a doubling of the room-temperature ZT, with a more modest increase of 40% being achieved at 720 K.

Table 2: Thermoelectric Performance Data for Tetrahedrite-Related Phases

Series	$(ZT)_{max}$	Temperature at which $(ZT)_{max}$ occurs/ K	Composition for $(ZT)_{max}$	Reference
$Cu_{12}Sb_4S_{13}$	0.76	623	----	135
	0.30	575	----	133
$Cu_{12-x}Ni_xSb_4S_{13}$	0.7	665	x = 1.5	131
$Cu_{12-x}Cr_xSb_4S_{13}$	1.0	700	x = 0.35	139
$Cu_{12-x}Co_xSb_4S_{13}$	0.94	723	x = 0.2	138
	0.98	673	x = 0.5	134
$Cu_{10.5}Ni_{1.5-x}Zn_xSb_4S_{13}$	1.03	723	x=0.5	144
$Cu_{12-x}Mn_xSb_4S_{13}$	1.13	575	x = 1.0	133
$Cu_{12-x}Cd_xSb_4S_{13}$	0.9	623	x = 0.75	136
$Cu_{12-x}Pb_xSb_4S_{13}$	0.8	723	x = 1.0	140
$Cu_{12-x}Ge_xSb_4S_{13}$	0.65	665	$0.3 \leq x \leq 0.5$	142
$Cu_{12-x}Mg_xSb_4S_{13}$	0.55	673	$0 \leq x \leq 1.5$	143
$Cu_{12}Sb_{4-x}Bi_xS_{13}$	0.84	673	x = 0.2	147
$Cu_{12}Sb_{4-x}Te_xS_{13}$	0.8	623	x= 0.61,0.80	146
	0.92	723	x = 1	145
$Cu_{12-x}Ni_x\ Sb_{4-y}Te_yS_{13}$	0.7	673	x = 0.5; y = 0.75	149
$Cu_{12-x}Ni_x\ Sb_{4-y}Te_yS_{13}$	0.80	700	x = 0.82; y = 0.41	148

While the majority of investigations have utilised high-temperature reaction of the elements or binary sulfides to prepare modified tetrahedrites, mechanochemical methods have also been applied.[153] Preparation of the stoichiometric ternary phase generally results in the presence of secondary phases, $Cu_{1.5}Sb_{0.5}S_2$ and Cu_3SbS_4.[154] A variable temperature powder X-ray diffraction study,[155] reveals the fractions of the three phases are relatively constant to 573 K, whilst above 673 K $Cu_{1.5}Sb_{0.5}S_2$ transforms into the chalcostilbite phase, $CuSbS_2$.

Above this temperature, there is a gradual decrease in the amount of the tetrahedrite phase, which disappears above 753 K, and an increase in the fraction of $CuSbS_2$, until that too disappears above 773 K. At high-temperatures, only the high-temperature form of skinnerite (Cu_3SbS_3) is present. Nickel substitution appears to stabilise the tetrahedrite structure. Diffraction data for $Cu_{12-x}Ni_xSb_4S_{13}$ (x = 1.5) reveal that only a tetrahedrite phase is present to 783 K, above which NiSbS and subsequently NiS begin to form, whereas at x=1.6, NiS can be identified even at room temperature, the proportion remaining constant to (at least) 673 K. This investigation demonstrates that at high temperature, a reaction mixture contains a number of non-tetrahedrite phases and the product composition on cooling to room temperature, will be affected by thermal history. This may be a contributor to variations in properties between the same non-stoichiometric series of materials prepared in different laboratories that is evident from Table 2. For example, ZT = 0.76 at 623 K determined for the parent phase, $Cu_{12}Sb_4S_{13}$, during an investigation of the effect of Mn doping,[135] is significantly greater than the ZT = 0.30 at 575 K determined previously,[133] whereas Mn-substituted phases show lower performance than in the earlier study.[133] The differences in performance of Mn-substituted materials may be due to slight compositional changes, which impact on the electrical properties, and a low sample density in the earlier study, which significantly reduces κ. Even those materials prepared in a single laboratory exhibit chemical compositions that depend on the details of the synthetic process.[146] Different amounts of secondary phases will lead to slight variations from nominal composition of the tetrahedrite phase, leading to the creation of defects that impact on charge-carrier concentration and hence transport properties.

The origin of the exceptionally low thermal conductivity in the highly-crystalline tetrahedrites has been the subject of considerable investigation and debate. Both natural and synthetic samples of tetrahedrites exhibit low-energy localised vibrational modes.[156] Calculation of the partial phonon density of states,[131] analysis of the temperature dependence of atomic displacement parameters[157] and high-angle annular dark-field (HAADF) imaging by STEM[158] support the view that these modes may be assigned to displacements of trigonally-coordinated copper ions. Such localised modes scatter acoustic phonons and hybridize with acoustic dispersions, resulting in reduced group velocities, thereby providing a mechanism for lowering thermal conductivity similar to that observed in PGEC materials. The absence in tetrahedrites of the atomic cages characteristic of PGEC materials has led to the suggestion that anharmonicity results from the electrostatic interaction associated with

stereochemically-active antimony lone pairs.[157] This leads to a weak interaction between copper at the centre of a CuS_3 trigonal planar unit, and two neighbouring atoms to create a Sb-(CuS_3)-Sb trigonal bipyramid (Figure 8), effectively creating a 5-coordinate cage, which would facilitate PGEC-type behaviour, in which the Cu-Sb distances fluctuate between lone pair and covalent bonding. This induces localized anharmonic motion of copper in an out-of-plane direction. However, it has also been suggested[159] that while the out-of-plane vibration is sensitive to the local environment of the copper at the centre of this cage, lone pairs play a less significant role and that the vibration is consequence of chemical pressure exerted in the (Cu)S_3 triangle, since the energy of the low-energy mode is decreased when the area of the (Cu)S_3 triangle is reduced.

Copper rich compositions, $Cu_{12+x}Sb_4S_{13}$ (x = 0.3, 2.0), consist of two closely-related tetrahedrite-type phases at room temperature.[160] For each value of x, one of the phases has a copper content in excess of 12, requiring the partial occupancy by excess copper of a normally-vacant trigonal planar (CuS_3) site, located in the windows of the sodalite cages. On heating, phase coalescence into a single tetrahedrite phase occurs in the temperature range $493 \leq T/K \leq 553$.[160] Inspection of the crystallographic composition, determined by Rietveld analysis of powder neutron diffraction data, reveals that at high temperatures, the material is copper deficient, although there is no evidence for the formation of impurity phases. This suggests delocalization of copper ions on heating, the onset of which is evident in structural data collected above 393 K, in contrast with the behaviour of the stoichiometric phase, for which there is no evidence of Cu-ion mobility in high-temperature neutron diffraction data.[161] Analysis of atomic displacement parameters[160] suggest the presence of low energy phonon modes associated with trigonal-planar copper ions, analogous to those identified in the stoichiometric material.[131,156] Excess copper reduces the thermal conductivity significantly: a value of $\kappa = 0.44$ W m^{-1} K^{-1} being determined at room temperature. Above the onset of copper ion mobility, the lattice contribution is nearly temperature-independent and below the glass-like minimum, which may be estimated[92] as 0.5 W m^{-1} K^{-1}. This exceptionally low thermal conductivity may be associated with the emergence of a liquid-like copper sub-lattice on heating, which leads to a softening of phonon modes and conferring PLEC character on the copper-rich tetrahedrites.

The exsolution into two closely-related phases identified in copper-rich compositions is widely observed in tetrahedrites and provides an effective mechanism for reducing the

thermal conductivity. At low Te contents ($x \approx 0.6$ - 0.8), $Cu_{12}Sb_{4-x}Te_xS_{13}$ prepared by high-temperature reaction of the binary sulfides, exsolves into two tetrahedrite phases on cooling below *ca*. 250 K.[162] Exsolution is accompanied by an increase in resistivity and a marked drop of *ca*. 40 % in thermal conductivity; κ reaching the remarkably low value of 0.25 W m^{-1} K^{-1} at temperatures below 200 K; again well below the estimated minimum thermal conductivity. The occurrence of phase coalescence at 200 K, limits exploitation of the exceptionally low thermal conductivity in practical applications. However, Yan et al[163] show that in $Cu_{12+x}Sb_4S_{13}$ ($x = 0.5, 1.0, 1.5$) two-phase behaviour and hence low thermal conductivity persists to *ca*. 700 K, although the difference in behaviour to that observed in the previous neutron study[160] is not clear. This leads to ZT = 1.0 at 723 K for x = 1.5, which is increased slightly to ZT = 1.1 at the same temperature, through the use of band engineering in $Cu_{13.5}Sb_4S_{12}Se$.

5. Conclusions and Future Prospects

There now exists several families of sulfides that show promising thermoelectric performance in the mid-range of temperatures (Figure 9), where Bi_2Te_3 is no longer suitable, even if issues of sustainability were to be addressed. In particular, in the range $500 \leq T/K \leq 800$, which encompasses that applicable to waste heat in industrial processes, materials in the tetrahedrite and $Cu_{2-x}S$ families have figures-of-merit that exceed unity in this range, with some examples reaching ZT > 1.5 at higher temperatures. However, what is readily apparent from Figure 9 is the dearth of *n*-type materials. All of the high-performance copper-sulfide-based materials that exhibit a thermoelectric figure-of-merit of ZT > 0.6 in the mid-range of temperatures are *p*-type semiconductors. Chalcopyrite affords a rare example of *n*-type behaviour but ZT remains comparatively low, typically achieving values only 20-30% of those of their *p*-type counterparts. Considerable effort will be required to develop new *n*-type materials of comparable performance, if an all-sulfide thermoelectric device is to be created. The application of high-throughput screening methods[164] may prove beneficial in the search for candidate materials.

The majority of investigations have tended to focus on producing materials with the highest maximum figure-of-merit and some spectacular advances have been achieved in *p*-type sulfides. However, device efficiency (η, defined as the ratio of the energy supplied to the load to the heat energy absorbed at the hot junction), is approximated by Eq. 2,[165] where $\overline{ZT}$ is the

average figure-of-merit of the device over the range T_c to T_h and T_c and T_h denote the temperatures of the cold and hot sides of the device respectively.

$$\eta = \frac{T_h - T_c}{T_h}\left[\frac{\sqrt{1+\overline{ZT}}-1}{\sqrt{1+\overline{ZT}}+\frac{T_c}{T_h}}\right] \quad \text{Eq. 2}$$

This expression represents the general case, where all three terms that contribute to Z (S, σ and κ) are temperature independent. This is seldom achieved in practice and optimum device performance requires a high average ZT for each of the component materials to be achieved over the temperature gradient of the thermoelements. An increase in this average ZT of *n*- and *p*-type materials would have a greater impact on efficiency than simply raising the maximum figure-of-merit. This is particularly true for systems where ZT(T) shows a sharp upturn at an intermediate temperature either as the result of a phase transition or due to phase exsolution or segregation. The materials described here adopt cubic structures or slightly distorted variants thereof and bonding anisotropy is expected to be low. In cases where there is significant anisotropy, reliable assessment of likely device performance will require electrical and thermal transport properties to be mesaured in the same direction on the consolidated material.

Materials stability is potentially a concern for sulfide-based thermoelectrics. Whilst aerial oxidation does not appear to be a significant problem in the likely temperature range of operation, sulfur volatilization during synthesis and consolidation frequently occurs. This produces compositional changes that have a marked influence on the electrical-transport properties in particular. Slight compositional changes due to the loss of sulfur, leading to deviations from nominal stoichiometries, are likely to lie behind the problems with achieving reproducibility in properties that are evident in several sulfide systems. Detailed chemical analysis is required to determine the true chemical composition of products. Further sulfur loss during operation of a thermoelectric device at elevated temperatures would potentially result in materials degradation and fall-off in performance. In extreme cases, sulfur loss induces the exsolution of one or more impurity phases, although the presence of these adventitious phases is not always deleterious to performance as they can form microprecipitates that scatter phonons effectively, thereby reducing the thermal conductivity.

In addition to sulfur volatilization, categories of thermoelectric material that depend on the emergence of a liquid-like sub-lattice to effect substantial reductions in thermal conductivity

also suffer from problems with stability under operating conditions. Under the electric field created when the device is subjected to a temperature gradient during operation, the mobile copper ions migrate and plate out at one end of the thermoelement, leading to compositional changes, cracking and loss of performance.[94] Extended current-stress testing, using large current densities, and the evaluation of the degree of reproducibility in performance on repeated cycling are clearly required for any genuine candidate materials for a new generation of thermoelectric device. An effective strategy to minimise the impact of this behaviour, without losing the benefits of a low thermal conductivity is the introduction of non-diffusing cations to block the migration path of the diffusing species. In bornite, where iron cations replace a fraction of the copper at tetrahedral positions, this leads to good reproducibility in thermoelectric behaviour on repeated heating and cooling,[109] albeit over a relatively small number of cycles. An alternative approach recently reported by Qiu et al,[166] is to tune the geometry of the thermoelectric legs in the device to ensure that the voltage difference across the PLEC material remains below a threshold value for stable operation. In particular, the minimum value for the ratio of cross-sectional areas of *p*- and *n*-type legs, A_p/A_n, in order to remain below the critical voltage for metal deposition was identified. The thermoelectric module constructed according to this principle, from the *p*-type PLEC, Cu_2Se, and the *n*-type filled skutterudite $Yb_{0.3}Co_4Sb_{12}$, shows good stability over > 400 h of operation and achieves a maximum efficiency of η_{max} = 9.1% at ΔT = 953 K. Significantly, similar considerations of A_p/A_n for a module containing the sulfide analogue, $Cu_{1.97}S$, suggests stable operation is restricted to ΔT = 200 K.

Device construction presents formidable technical and scientific challenges as materials that have been developed for a given family of materials may not be transferable to a new materials system. For example, recent work by Chetty et al[167] has shown that several common diffusion barrier materials, including Ni and Ti, are incompatible with the colusite-type phase $Cu_{26}Nb_2Ge_6S_{32}$. A monocouple was successfully constructed using a gold diffusion barrier with a low contact resistance allowing a maximum thermoelectric conversion efficiency of η = 3.3% to be realised. Large-scale implementation of thermoelectric technology will also require production of large volumes of material with reproducible properties, which itself presents manufacturing challenges. While naturally-occurring chalcopyrite[54] and tetrahedrites[168] have been shown to offer a direct source of thermoelectric material, the highest performance requires a degree of control over composition and microstructure that can only be achieved in a synthetic material. The majority of copper sulfides investigated to

date have been prepared by high-temperature synthesis, typically in sealed, evacuated fused silica ampoules. This has inherent limitations on scale, restricting the amounts of material to < 20 g. Both mechanochemical[153] and solution-based methods[169,170] have been investigated as alternative scalable synthetic routes to tetrahedrites and each has been shown to produce material with comparable performance to that produced by small-scale high-temperature synthesis. Similarly, up-scaling consolidation by SPS has also been achieved.[171] The performance of high density $50 \times 50 \times 3$ mm^3 monoliths of the tetrahedrite, $Cu_{10.4}Ni_{1.6}Sb_4S_{13}$ produced in this way is comparable with that of materials produced by conventional laboratory-scale SPS.

In conclusion, the spectacular advances in the performance of copper sulfide thermoelectrics achieved over the last 5 - 6 years has resulted in a range of *p*-type materials with high ZT in the mid-range of temperatures. The majority of the systems present greater complexity than is often evident from their relatively simple chemical formulae, with phase segregation, compositional changes and phase transitions all having an impact on thermoelectric properties. Implementation of these new materials in all-sulfide thermoelectric devices requires formidable challenges to be overcome, not least the discovery of a compatible high-performance *n*-type sulfide and resolving issues of materials' stability under operating conditions. The devices themselves will require compatible solders and other materials required for module construction to be identified, while assessment of mechanical properties for candidate materials for device applications in which modules are exposed to vibrations will be required. However if such challenges are overcome, copper sulfides have the potential to address a pressing need for materials able to operate in the technologically-important mid-range of temperatures for energy harvesting from waste heat.

Figure Captions

Figure 1 (a) Schematic representation of the operation a thermoelectric couple composed of *n*- and *p*-type thermoelements and (b) A 30 × 30 mm^2 thermoelectric module composed of an array of thermoelectric couples connected electrically in series and thermally in parallel.

Figure 2 Schematic representation on the changes to band structure expected in the region of the Fermi level on progressing from sulfide to selenide to telluride, illustrating the increase in VB width and corresponding decrease in effective mass of the carriers, in this case holes, and narrowing of the band gap.

Figure 3 The relationship between the structures of copper sulfide phases derived from CuS_4 tetrahedra (red polyhedra). Although the simple zinc-blende structure, obtained by vertex linking metal-centred tetrahedra is not adopted by the binary sulphide, the cation ordered derivatives chalcopyrite, stannite or kesterite result when other tetrahedrally-coordinated cations are introduced in addition to copper. Occupation of the otherwise empty tetrahedral sites in the zinc-blende structure (translucent magenta polyhedral) generates the antifluorite structure, which $Cu_{2-x}S$ and related phases adopt at high temperatures.

Figure 4 Vacancy ordering in the three phases of Cu_5FeS_4. (a) Ambient temperature (4a) phase, viewed along [100]; (b) intermediate temperature (2a) phase viewed along [100] and (c) perspective view of the high temperature phase, in which there is a statistical distribution of copper and iron cations and cation vacancies at the centre of each tetrahedron. $(Cu,Fe)S_4$ tetrahedra in the antifluorite sub-cells of (a) and (b) are shown as red polyhedra, whilst copper/iron ions in the zinc blende sub-cells are represented by red spheres. Sulfide anions are represented by yellow spheres. To aid clarity, only slices of thickness *a*/4 are shown in (a) and (b).

Figure 5 The structure of colusite $Cu_{26}V_2Ge_6S_{32}$ (a) the network of vertex-linked CuS_4 (red) and GeS_4 (cyan) tetrahedra, with vanadium cations and sulfide anions shown as magenta and yellow spheres respectively; (b) the body-centred-cubic array of vanadium-centred tetrahedra (magenta), with copper cations and sulphide anions shown as red and

yellow spheres respectively.

Figure 6 The structure of tetrahedrite $Cu_{12}Sb_4S_{13}$. (a) View along [100], with CuS_4 tetrahedra in red, CuS_3 trigonal-planar units in blue and antimony and sulfur atoms represented by magenta and yellow spheres respectively; (b) Linkage of CuS_4 tetrahedra to create a sodalite-like cage, highlighted by solid black lines; (c) Representation of the sodalite cage, with copper atoms at the centres of CuS_4 tetrahedra shown as red spheres, containing the "spinner" derived from octahedral coordination of sulfur (yellow spheres) by six CuS_3 trigonal-planar units (blue).

Figure 7 Schematic illustration (after reference 90) of PLEC behaviour in $Cu_{2-x}S$ phases at elevated temperatures, where Cu-ion mobility results in a liquid like sub-lattice, represented as a red continuum, whilst the sulfide anions (yellow spheres) remain localised in a face-centred cubic arrangement.

Figure 8 The Sb-(CuS_3)-Sb trigonal-bipyramidal unit in the tetrehedrite structure, discussed in the text. Atoms of the average structure are denoted as solid spheres (Cu: red; sulfur; yellow; antimony: magenta), with the long (*ca*. 3.4 Å) interactions shown as red lines. The translucent red spheres represent copper ions in the split-site model that has been used**Error! Bookmark not defined.** to model the displacement (represented schematically by the double headed arrow) associated with fluctuation of Cu-Sb distances.

Figure 9 The maximum figure-of-merit, $(ZT)_{max}$, obtained for the families of copper sulphides, discussed in Section 4, and the temperature at which it occurs. All materials are *p*-type unless stated otherwise.

Figure 1

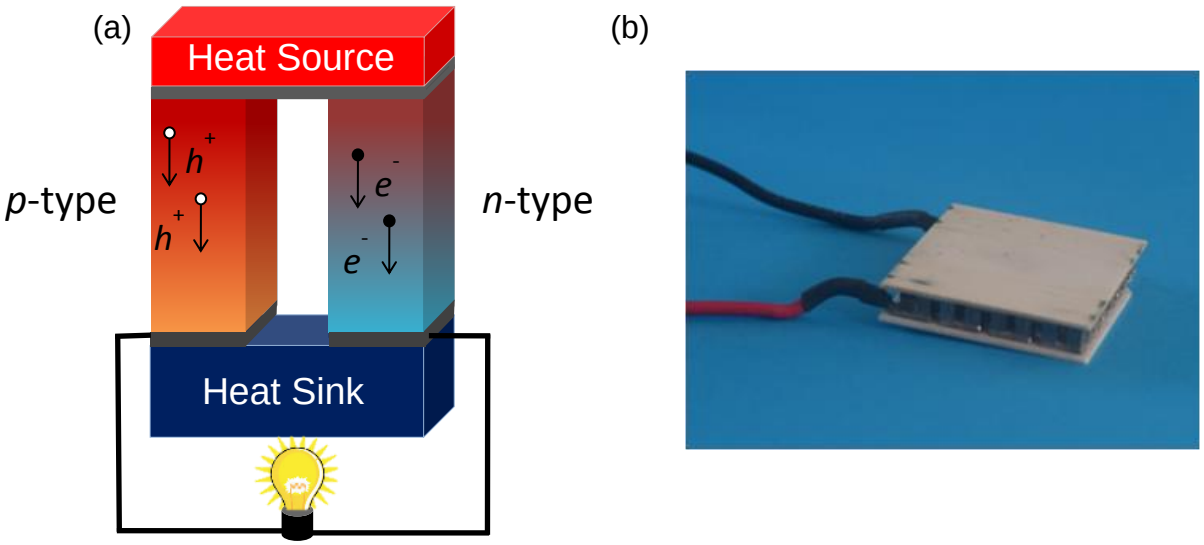

Figure 2

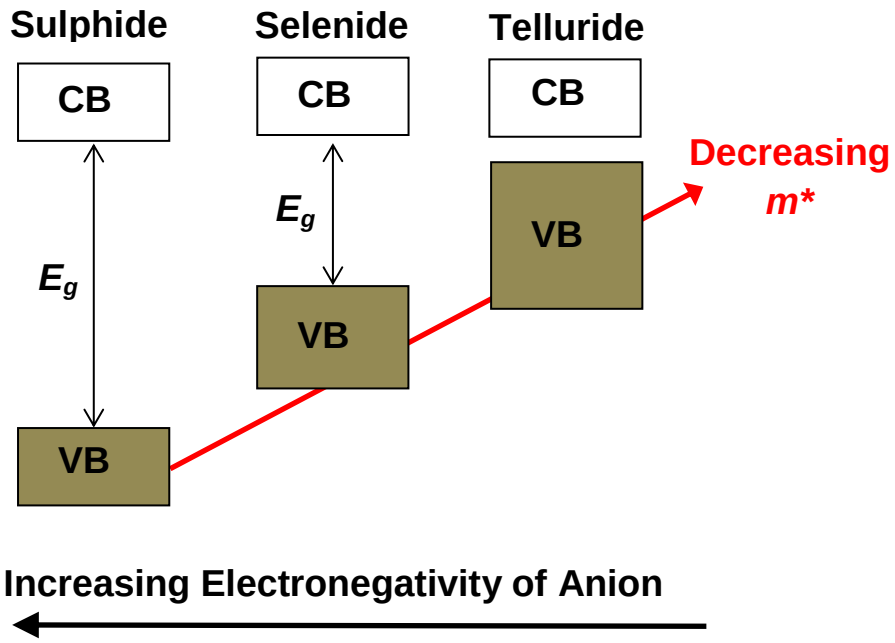
Sulphide
Selenide
Telluride
CB
CB
CB
E_g
E_g
VB
VB
VB
Decreasing
m*
Increasing Electronegativity of Anion

Figure 3

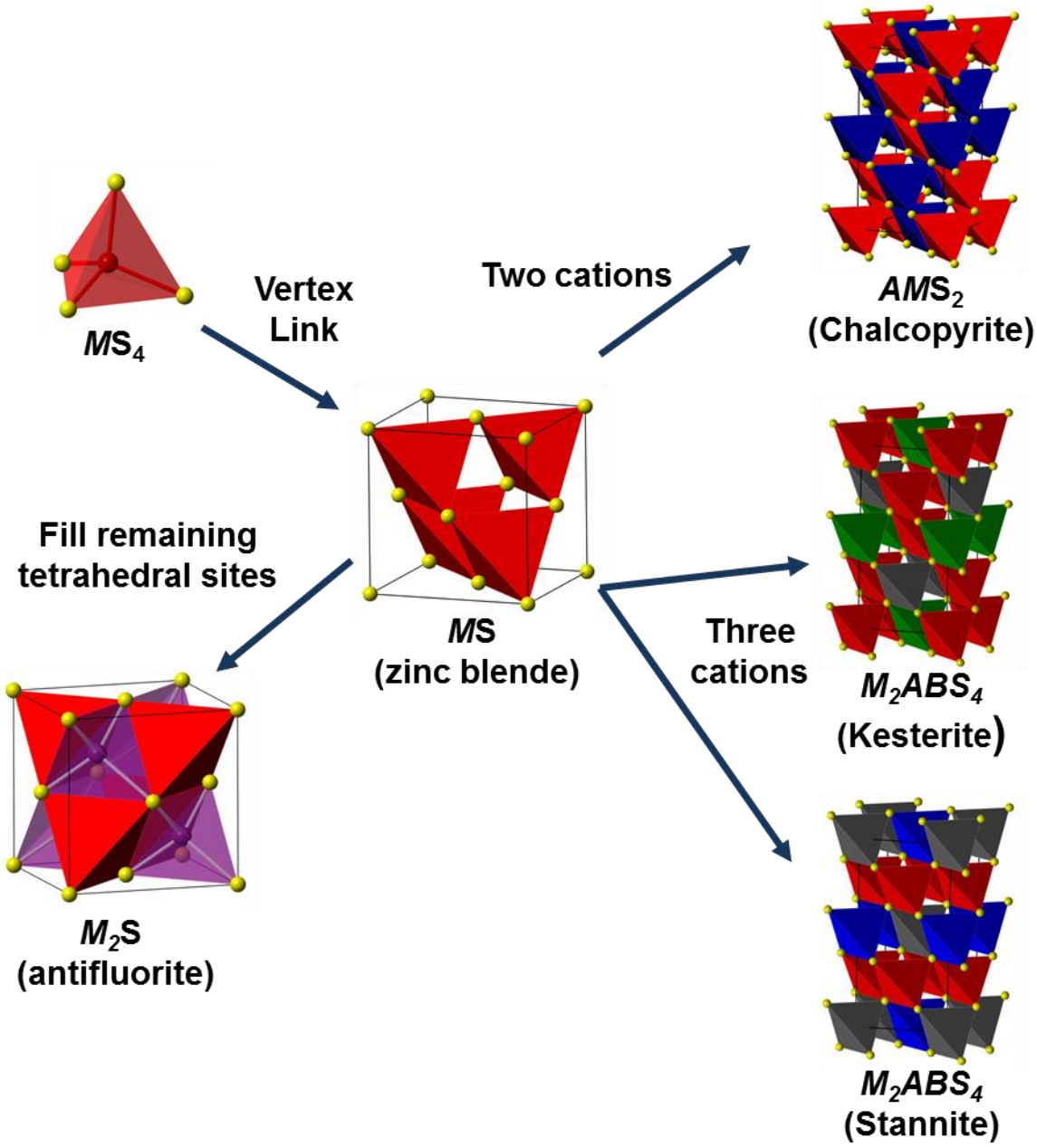
MS_4
Vertex
Link
Two cations
AMS_2
(Chalcopyrite)
Fill remaining
tetrahedral sites
MS
(zinc blende)
Three
cations
M_2ABS_4
(Kesterite)
M_2S
(antifluorite)
M_2ABS_4
(Stannite)

Figure 4

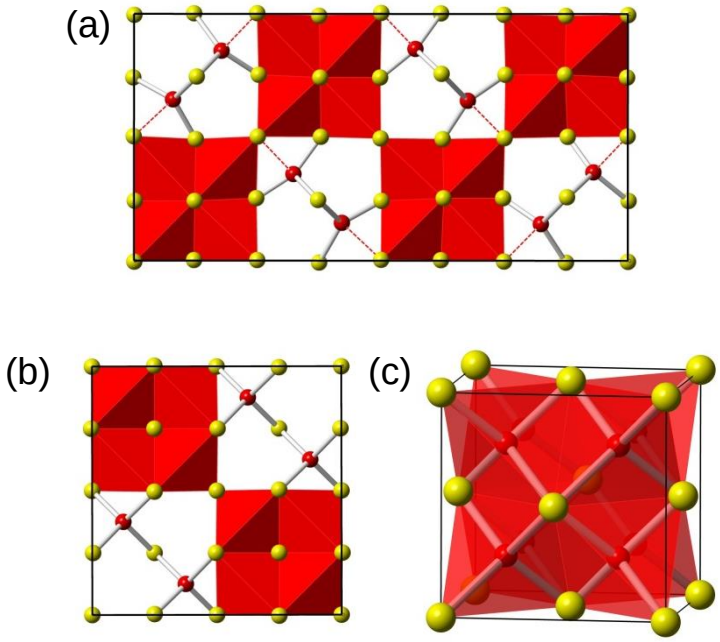

Figure 5

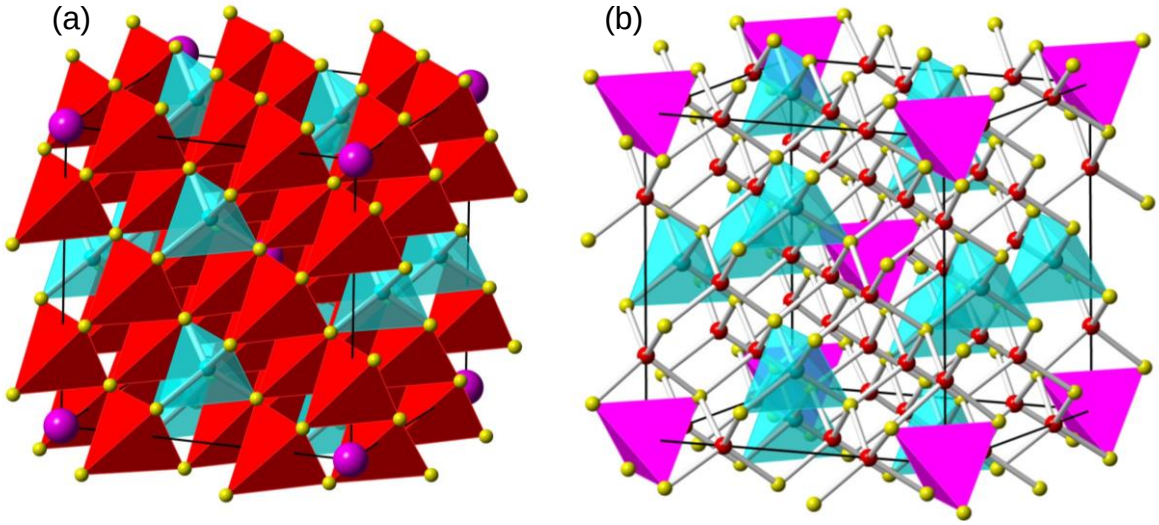

Figure 6

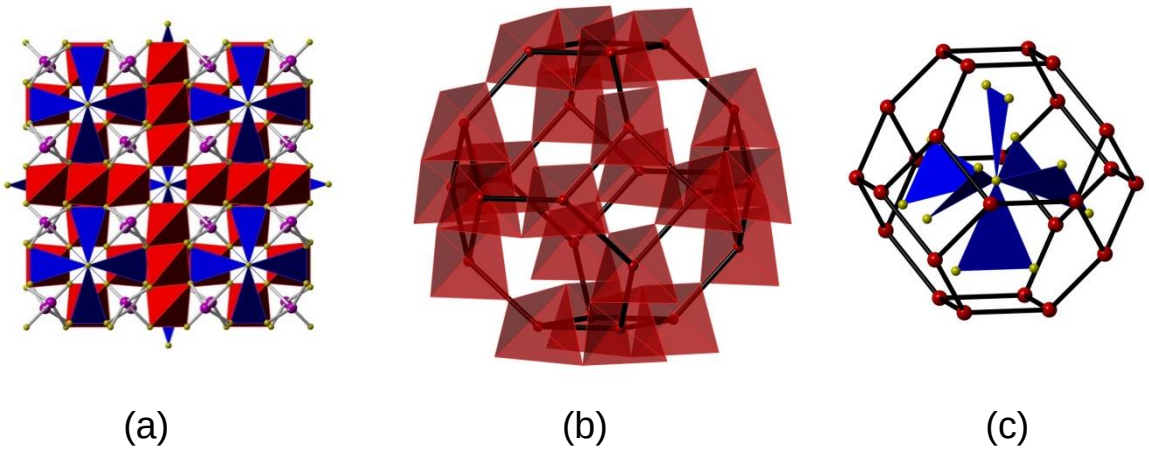

(a) (b) (c)

Figure 7

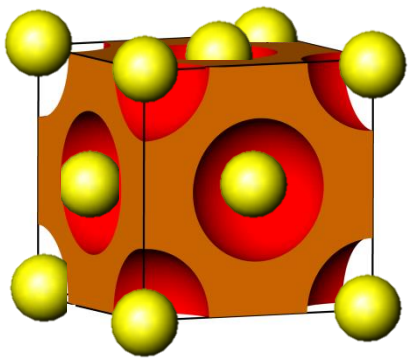

Figure 8

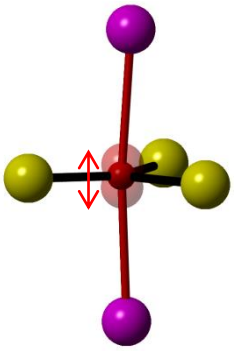

Figure 9

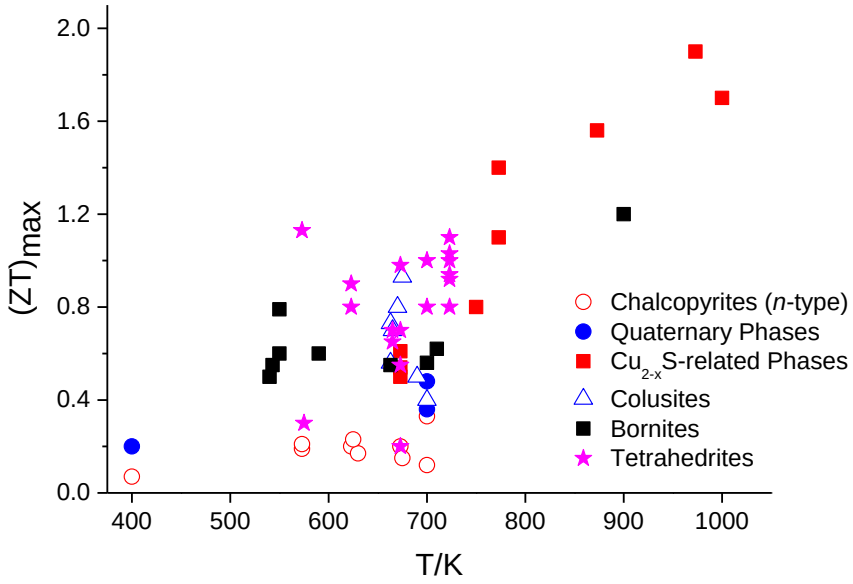
2.0
1.6
1.2
0.8
0.4
0.0
(ZT)max
400
500
600
700
800
900
1000
T/K
Chalcopyrites (n-type)
Quaternary Phases
Cu2-xS-related Phases
Colusites
Bornites
Tetrahedrites

References

[1] A.V. Powell and P. Vaqueiro, in *Thermoelectric Materials and Devices*, Ed. I. Nandhakumar, N. M. White, S. Beeby, Royal Society of Chemistry, Cambridge, Ch. 2, p. 27, (2017).

[2] LD. Zhao, J. He, D. Berardan, Y. Lin, JF. Li, CW. Nan and N. Dragoe, *Energy Environ. Sci.*, **7**, 2900, (2014).

[3] S Hébert, D. Berthebaud, R Daou, Y Bréard, D Pelloquin, E Guilmeau, F Gascoin, O Lebedev, A Maignan, *J. Phys. Condens. Mat.*, **28**, 013001, (2016).

[4] M. Rull-Bravo, A. Moure, J.F. Fernandez and M. Martin-Gonzalez, *RSC Adv.*, **5**, 41653, (2015).

[5] J.W.G Bos and R.A. Downie, *J. Phys: Condens Mat.*, **26**, 433201, (2014).

[6] S. Toberer, A.F. May and G.J. Snyder, *Chem. Mater.*, **22**, 624, (2010).

[7] J. Mao, H. Zhu, Z. Ding, Z. Liu, G. A. Gamage, G. Chen and Z. Ren, *Science*, **365**, 495, (2019).

[8] H. Kleinke, *Chem. Mater.*, **22**, 604, (2010).

[9] T. Takabatake in *Thermoelectric Nanomaterials*, Ed. K. Koumoto and T. Mori, Springer, Heidelbrg, Ch. 2, p. 33, (2013).

[10] A. Nozariasbmarz, A. Agarwal, Z.A. Coutant, M. J. Hall, J. Liu, R. Liu, A. Malhotra, P. Norouzzadeh, M. C. Öztürk, V. P. Ramesh, Y. Sargolzaeiaval, F. Suarez and D. Vashaee, *Jpn. J. Appl. Phys.*, **56**, 05DA04, (2017).

[11] G. Tan, L-D Zhao, and M.G. Kanatzidis, *Chem. Rev.*, **116**, 12123, (2016).

[12] G. A. Slack, in *CRC Handbook of Thermoelectrics*, Chapter 34, p. 407, Ed. D. M. Rowe, CRC Press, Boca Raton, (1995).

[13] M.G. Kanatzidis, *Chem. Mater.*, **22**, 648, (2010).

[14] LD. Zhao, BP. Zhang, JF. Li, M. Zhou, WS. Liu and J. Liu, *J. Alloys Compnd.*, **455**, 259, (2008).

[15] S. II Kim, K.H. Lee, H.A. Mun, H.S. Kim, S.W. Hwang, J.W. Roh, D.J. Yang, W.H. Shin, X.S. Li, Y.H. Lee, G.J. Snyder and S.W. Kim, *Science*, **348**, 109, (2015).

[16] L.D. Hicks and M.S. Dresselhaus, *Phys. Rev. B*, **47**, 16631, (1993).

[17] J .P. Heremans, B. Wiendlocha and A. M. Chamoire, *Energy Environ. Sci.*, **5**, 5510, (2012).

[18] B. Liu, J. Hu, J. Zhou and R. Yang, *Materials*, **10**, 418, (2017).

[19] J-B. Vaney, S. Aminorroaya Yamini, H. Takaki, K. Kobayashi, N. Kobayashi and T. Mori, *Mater. Today. Phys*., **9**, 100090, (2019).

[20] N. Tsujii, A. Nishide, J. Hayakawa and T. Mori, *Sci. Adv*., **5**, eaat5935, (2019).,

[21] H. Liu, X. Shi, F. Xu, L. Zhang, W. Zhang, L. Chen, Q. Li, C. Uher, T. Day and G. J. Snyder, *Nat. Mater.*, **11**, 422, (2012).

[22] X. Shi, J. Yang, J. R. Salvador, M. Chi, J. Y. Cho, H. Wang,S. Bai, J. Yang, W. Zhang and L. Chen, *J. Am. Chem. Soc*., **133**, 7837, (2011).

[23] K. Biswas, J. He, I.D. Blum, CI. Wu, T.P. Hogan, D.N. Seidman, V.P. Dravid and M.G. Kanatzidis, *Nature*, **489**, 414, (2012).

[24] LD. Zhao, SH. Lo, Y. Zhang, H. Sun, G. Tan, C. Uher, C. Wolverton, V.P. Dravid and M.G. Kanatzidis, *Nature*, **508**, 373, (2014).

[25] T. Kajikawa, in *Thermoelectrics Handbook: Macro to Nano*, ed. D.M. Rowe, CRC Press, Boca Raton, Ch. 50, p. 804, (2006).

[26] E.S. Toberer, C.A. Cox, S.R. Brown, T. Ikeda, A. F. May, S. M. Kauzlarich and G. J. Snyder, *Adv. Func. Mater*., **18**, 2795, (2008).

[27] G.J. Snyder and E.S. Toberer, *Nat. Mater.*, **7**, 105, (2008).

[28] K. Suekuni and T. Takabatake, *APL Mater*., **4**, 104503, (2016).

[29] P. Ren, Y. Liu, J. He, T. Lv, j. Gao and G. Xu, *Inorg. Chem. Front*. **5**, 2380, (2018).

[30] Z-H Ge, L-D. Zhao, D. Wu, X. Liu, B-P. Zhang, J-F. Li and J. He, *Mater. Today*, **19**, 227, (2016).

[31] R. Chetty, A. Balie, and R.C. Mallik, *J. Mater. Chem. C*, **3**, 12364, (2015).

[32] E. Davies, *Chem. World*, **8**, 50, (2011).

[33] U.S. Geological Survey, 2019 Mineral commodity summaries 2019: U.S. Geological Survey, 200 p., https://doi.org/10.3133/70202434.

[34] W.G. Zeier, A. Zevalkink, Z.M. Gibbs, G. Hautier, M.G. Kanatzidis and G.J. Snyder, *Angew. Chem*., **55**, 6826, (2016).

[35] T. Zhao, Y-A. Wang, Z-Y. Zhao, Q. Liu and Q-J. Liu, *Mater. Res. Express*, **5**, 016305, (2018).

[36] *CRC Handbook of Chemistry and Physics*, 87th Edition, Taylor & Francis, Boca Raton, (2006).

[37] H.T Evans and J.A. Konnert, *Am. Mineral*., **61**, 996, (1976).

[38] I. Tsuji, Y. Shimodaira, H. Kato, H. Kobayashi and A. Kudo, *Chem. Mater*, **22**, 1402, (2010).

[39] S. Siebentritt and S. Schorr, *Prog. Photovolt. Res. Appl*., **20**, 512, (2012**)**.

[40] S. Schorr, *Sol. Energy Mater. Sol. Cells*, **95**, 1482, (2011).

[41] P. Mangelis, A. Aziz, I. da Silva, R. Grau-Crespo, P. Vaqueiro and A. V. Powell, *Phys. Chem. Chem. Phys*, in press DOI:. 10.1039/C9CP03630J

[42] D.J. Chakrabarti and D.E. Laughlin, *Bull. Alloy Phase Diagrams*, **4**, 254, (1983).

[43] P. Qiu, Y. Zhu, Y. Qin, X. Shi and L. Chen, *APL Mater*, **4**, 104805, (2016).

[44] Y. Kanazawa, K. Koto, and N. Morimoto, *Can. Mineral*. **16**, 397, (1978).

[45] N. Morimoto, *Acta Cryst.* **17**, 351, (1964).

[46] B.A. Grguric, A. Putnis and R.J. Harrison, *Am. Mineral*., **83**, 1231, (1998).

[47] B.Y.K Koto and N. Morimoto, *Acta Cryst.*, **3**1, 2268, (1975).

[48] A. Martinelli, G.O. Lepore, F. Berardini, A. Giaccherini and F. Di Benedetto, *Acta Cryst Section B*, **874**, 405, (2018).

[49] P.G. Spry, S. Merlino, S. Wang, X. Zhang and P.R. Buseck, *Am. Miner.*, **79**, 750, (1994).

[50] E. Makovicky, *Rev. Mineral. Geochem.*, **61**, 7, (2006).

[51] N.E. Johnson, J.R. Craig and J.D. Rimstidt, *Am. Miner.*, **73**, 389 (1988).

[52] T-R. Wei, Y. Qin, T. Deng, Q. Song, B. Jiang, R. Liu, P. Qiu, X. Shi and L. Chen, Sci. China Mater., **62**, 8, (2019).

[53] P. Wyzga, M. Bobnar, C. Hennig, A. Leithe-Jasper, T. Mori and R. Gumeniuk, *Z Anorg. Allg. Chem*., **643**, 858, (2017).

[54] R. Ang A..U. Khan, N. Tsujii, K. Takai, R. Nakakmura and T. Mori, *Angew Chem. Int Ed.*, **54**, 12909, (2015).

[55] N. Tsujii and T. Mori. *Appl. Phys. Express*, **6**, 043001, (2013).

[56] H. Takaki, K. Kobayashi, M. Shimono, N. Kobayashi, K. Hirose, N. Tsujii and T. Mori, *Appl. Phys. Lett*. **110**, 072107, (2017).

[57] J. Park. Y. Xia and V. Ozoliņš, *J. Appl. Phys*., **125**, 125102, (2019).

[58] N. Tsujii, *J. Electron Mater*., **42**, 1974, (2013).

[59] N. Tsujii, T. Mori and Y. Isoda, *J Electron Mater*, **43**, 2371, (2014).

[60] N. Tsujii. F. Meng, K. Tsuchiya, S. Maruyama and T. Mori, *J. Electron Mater*., **45**, 1642, (2016).

[61] H. Takaki, K. Kobayashi, M. Shimono, N. Kobayashi, K. Hirose, N. Tsujii and T. Mori *Mater. Today Phys*. **3**, 85, (2017).

[62] Y. Li, T. Zhang, Y. Qin, T. Day, G.J. Snyder, X. Shi and L. Chen, *J. Appl. Phys*. **116**, 203705, (2014).

[63] D. Berthebaud, O.I. Lebedev and A. Maignan, *J. Materiomics*, **1**, 68, (2015).

[64] R. Lefevre, D. Berthebaud, M-Y. Mychinko, O.I. Lebedev, T. Mori, F. Gascoin and A. Maignan, *RSC Adv.*, **6**, 55117, (2016).

[65] J. Navratil, J. Kasparova, T. Plechacek, L. Benes, Z. Olmrova-Zmrhalova, V. Kucek and C. Drasar, *J. Electron Mater*., **48**, 1795, (2019).

[66] H. Xie, X. Su, G. Zheng, T. Zhu, K. Yin, Y. Yan, C. Uher, M.G. Kanatzidis and X. Tang, *Adv Energy Mater*., **7**, 1601299, (2017).

[67] H. Xie, X. Su, G. Zheng, Y. Yan. W/ Liu, H. Tang, M.G. Kanatzidis, C. Uher and X. Tang, *J. Phys. Chem. C*, **120**, 27895, (2016).

[68] J.D. Burnett, O. Gourdon, J.G.S. Ranmohotti, N.J. Takas, H. Dijeutedjeu, P.F.P. Poudeu and J.A. Aitken, *Mater. Chem Phys*., **147**, 17 (2014).

[69] J. Li. Q. Tan, amd J-F. Li, *J. Alloy Compd.*, **551**, 143, (2013).

[70] W.D. Carr and D.T. Morelli, *J. Electron Mater*, **45**, 1346, (2016).

[71] M. Singh, M. Miyata, S. Nishino, D. Mott, M. Koyano and S. Maenosono, *Nanomaterials*, **5**, 1820, (2015).

[72] D. Liang, R. Ma, S. Jiao, G. Pang and S. Feng, *Nanoscale*, **4**, 6265, (2012).

[73] S. Verma, M. Singh, D. Ahuja, H. Shimose, S. Nishino, M. Miyata, D. Mott, M. Koyano and S. Maenosono, *Jpn. J. Appl. Phys*. **53**, 120301, (2014).

[74] H. Xie, X. Su, Y. Yan, W. Liu, L. Chem, J. Fu, J. Yang, C. Uher and X. Tang, *NPG Asia Mater.*, **9**, e390, (2017).

[75] X. Y. Shi, F. Q. Huang, M. L. Liu, and L. D. Chen, *Appl. Phys. Lett*. **94**, 122103, (2009).

[76] M-L. Liu, I-W. Chen, F-Q. Huang and L-D. Chen, *Adv Mater*., **21**, 3808, (2009).

[77] Y. Dong, H. Wang and G. S. Nolas, *Inorg. Chem*., **52**, 14364, (2013).

[78] Y. Dong, L. Wojtas, J. Martin and G. S. Nolas, *J. Mater. Chem C*, **3** 10436, (2015).

[79] C. Sevik and T. Çağin, *Appl. Phys. Lett*, **95**, 112105, (2009).

[80] C. Sevik and T. Çağin, *Phys Rev. B*, **82**, 0452020, (2010).

[81] A. Nagaoka, T. Masuda, S. Yasui, T. Taniyama and Y. Nose, *Appl. Phys. Express*. **11**, 051203, (2018).

[82] H. Yang, L.A. Jauregui, G. Zhang, Y.P. Chen, and Y. Wu, *Nano Lett*., **12**, 540, (2011).

[83] M-L Liu, F-Q. Huang, L-D. Chen, and I-W. Chen, *Appl. Phys Lett*, **94**, 202103, (2009).

[84] C.P. Heinrich, T.W. Day, W.G. Zeier, G.J. Snyder and W. Tremel, *J. Am. Chem. Soc*, **136**, 442, (2013).

[85] A. Miglio, C.P. Heinrich, W. Tremel, G. Hautier and W.G. Zeier, *Adv. Sci*, **4**, 1700080, (2017).

[86] X. Zheng, Y. Liu, Y. Du, Y. Sun, J. Li, R. Zhang, Q. Li, P. Chen, G. Zhao, Y. Fang, and N. Dai, *J. Alloys Compd*., **738**, 484, (2018).

[87] A. Nagaoka, T. Masuda, S. Yasur, T. Taniyama and Y. Nose, *Jpn. J. Appl. Phys*. **57**, 101201, (2018).

[88] Y. Goto, F, Naito, R. Sato, K. Yoshiyasu, T. Itoh, Y. Kamihara and M. Matoba, *Inorg. Chem.*, **52**, 9861, (2013).

[89] T.P. Bailey and C. Uher, *Curr. Opin. Green Sustain. Chem*., **4**, 58 (2017).

[90] Y He, T. Day, T. Zhang, H. Liu, X. Shi, L. Chen and G.J. Snyder, *Adv Mater*, **26**, 3974, (2014).

[91] Y. Sun, L. Xi, J. Yang, L. Wu, S. Shi, L. Chen, G. Snyder, J. Yang and W. Zhang, *J. Mater Chem, A*, **5**, 5098, (2017).

[92] D.G. Cahill, S.K. Watson and R.O. Pohl, *Phys. Rev. B*, **46**, 6131, (1992).

[93] L. Zhao, W. Wang, F-Y. Fei, J. Wang, Z. Cheng, S. Dou, J. Wang and G.J. Snyder, *J. Mater. Chem. A*, **3**, 9432, (2015).

[94] G. Dennler, R. Chmielowski, S. Jacob, F. Capet, P. Roussel, S. Zastrow, K. Nielsch, I. Opahle and G.K.H. Madsen, *Adv. Energy Mater*., **4**, 1301581, (2014).

[95] Z-H Ge, B-P. Zhang, Y-X., Chen, Z-X. Yu and J-F. Li, *Chem Commun*, **47**, 12697, (2011).

[96] Z-H Ge, X. Liu, D. Feng, J. Lin and J. He, *Adv Energy Mater*., **6**, 1600607, (2016).

[97] D. Vasilevskiy, M.K. Keshavarz, J.-M. Simard, R.A. Masut, S. Turenne, and G.J. Snyder, *J. Electron. Mater*. **47**, 3314, (2018).

[98] D-D. Liang, B-P. Zhang and L. Zou, *J. Alloys Compd.*, **731**, 577, (2018).

[99] D-D. Liang, Z-H. Ge, H-Z Li, B-P. Zhang and F. Li, *J. Alloys Compd*, **708**, 169, (2017).

[100] Y-X Zhang, Z. Ma, Z-H. Ge, P. Qin, F. Zheng and J. Feng, *J. Alloys Compd*, **764**, 738, (2018).

[101] Z-H Ge, X. Chong, D. Feng, Y-X-. Zhang, Y. Qiu, L. Xie, P-W. Guan, J. Feng and J. He, *Mater. Today Phys.*, **8**, 71, (2019).

[102] P. Qin, Z-H. Ge, Y-X. Chen, X. Chong, J. Feng and J. He, *Nanotechnology*, **29**, 345402, (2018).

[103] H. Tang, F-H. Sun, J-F. Dong, Asfandiyar, H-L. Zhuang, Y. Pan and J-F. Li, *Nano Energy*, **49**, 267, (2018).

[104] Y-X Zhang, Z-H. Ge and J. Feng, *J. Alloy Compd*., **727**, 1076, (2017).

[105] M.G. Townsend, J.R. Gosselin, R.J. Tremblay, L.G. Ripley, D.W. Carson and W.B. Muir, *J. Phys. Chem. Solids*, **38**, 1153, (1977).

[106] M. Borgheresi, F.Di Benedetto, M. Romanelli,·M. Reissner, W. Lottermoser,· R.R. Gainov, R.R. Khassanov, G. Tippelt,·A. Giaccherini, L. Sorace, G. Montegrossi, R. Wagner and G. Amthauer, *Phys. Chem. Miner*., **45**, 227, (2018).

[107] P. Qiu, T. Zhang, Y. Qiu, X. Shi and L. Chen, *Energy Environ. Sci.*, **7**, 4000, (2014).

[108] G. Guélou, A.V. Powell and P. Vaqueiro, *J Mater. Chem C*, **3**, 10624, (2015).

[109] S.O.J. Long, A.V. Powell, P. Vaqueiro and S. Hull, *Chem. Mater*., **30**, 456, (2018).

[110] V. Pavan Kumar, T. Barbier, P. Lemoine, B. Raveau, V. Nassif and E. Guilmeau, *Dalton Trans*., **46**, 2174, (2017).

[111] A.O. Moghaddam, A. Shokuhfar and A. Cabot, *J. Alloy Compd*., **750**, 1, (2018).

[112] A.O. Moghaddam, A. Shokuhfar, P. Guardia, Y. Zhang and A. Cabot, *J. Alloy Compd*., **773**, 1064, (2019).

[113] A. Zhang, X. Shen, Z. Zhang, X. Lu, W. Yao, J. Dai, D. Xie, L. Guo, G. Wang and X. Zhou, *J. Mater. Chem. C*, **5**, 301, (2017).

[114] A. Zhang, B. Zhang, W. Lu, D. Xie, H. Ou, X. Han, J. Dai, X. Lu, G. Han, G. Wang and X. Zhou, *Adv. Func. Mater*., **28**, 1705117, (2018).

[115] M. Singh, P. Dwivedi, D. Mott, K. Higashimine, M. Ohta, H. Miwa, T. Akatsuka and S. Maenosono, *Ind. Eng. Chem. Res*., **58**, 3688, (2019).

[116] K. Suekuni, F.S. Kim, H. Nishiate, M. Ohta, H.I. Tanaka and T. Takabatake, *Appl. Phys. Lett*., **105**, 132107, (2014).

[117] C. Bourges, Y. Bouyrie, A.R. Supka, R.A.R. Al Orabi, P. Lemoine, O.I. Lebedev, M. Ohta, K. Suekuni, V. Nassif, V. Hardy, R. Daou, Y. Miyazaki, M. Fornari and E. Guilmeau, *J. Am. Chem. Soc.*, **140**, 2186, (2018).

[118] E.S. Toberer, A. Zevalkink and G.J.Snyder, *J. Mater. Chem.*, **21**, 15843, (2011).

[119] K. Suekuni, F.S. Kim and T. Takabatake, *J. Appl Phys*., **116**, 063706, (2014).

[120] F.S. Kim, K. Suekuni, H. Nishiate, M. Ohta, H.I. Tanaka and T. Takabatake, *J. Appl Phys*., **119**, 175105, (2016).

[121] C. Bourges, M. Gilmas, P. Lemoine, N.E. Mordvinova, O.I. Lebedev, E. Hug, V. Nassif, B. Malaman, R. Daou and E. Guilmeau, *J. Mater. Chem. C*, **4**, 7455, (2016).

[122] Y. Kikuchi, Y. Bouyrie, M. Ohta, K. Suekuni, M. Aihara, and T. Takabatake, *J. Mater. Chem. A*, **4**, 15207, (2016).

[123] P.G. Spry, S. Merlino, S. Wang, X. Zhang, P.R. Buseck, *Am. Miner.*, **79**, 750, (1994).

[124] K. Suekuni, Y. Shimizu, E. Nishibori, H. Kasai, H. Saito, D. Yoshimoto, K. Hashikuni, Y. Bouyrie, R. Chetty, M. Ohta, E. Guilmeau, T. Takabatake, K. Watanabe and M. Ohtaki, *J. Mater Chem A*, **7**, 228, (2019).

[125] Y. Bouyrie, V. Ohorodniichuk, S. Sassi, P. Masschelein, A. Dauscher, C. Candolfi and B. Lenoir, *J. Electron. Mater*., **46**, 2684, (2016).

[126] Y. Bouyrie. M. Ohta, K. Suekuni, Y. Kikuchi, P. Jood, A. Yamamoto and T. Takabatake, *J. Mater. Chem. C*, **5**, 4174, (2017).

[127] Y. Bouyrie, M. Ohta, K. Suekuni, P. Jood and T. Takabatake, *J. Alloy Compd*., **735**, 1838, (2018).

[128] S. Tippireddy, R. Chetty, M.H. Naik, M. Jain, K. Chattopadhyay and R.C. Mallik, *J. Phys. Chem. C*, **122**, 8735, (2018).

[129] K. Suekuni, K. Tsuruta, T. Ariga and M. Koyano, *Appl. Phys. Express*, **5**, 051201, (2012).

[130] K. Suekuni, Y. Tomizawa, T. Ozaki and M. Koyano, *J. Appl. Phys.*, **115**, 143702, (2014).

[131] X Lu, D.T. Morelli, Y. Xia, F. Zhou, V. Ozolins, H. Chi, X. Zhou and C. Uher, *Adv. Energy Mater*., **3**, 342, (2013).

[132] K. Suekuni, K. Tsuruta, M. Kunil, H. Nishiate, E. Nishibori, S. Maki, M. Ohta, A. Yamamoto and M. Koyano, *J Appl. Phys.*, **113**, 043712, (2013).

[133] J. Heo, G. Laurita, S. Muir, M.A. Subramanian and D.A. Keszler, *Chem. Mater.*, **26**, 2047, (2014).

[134] R. Chetty, A. Bali, M.H. Naik, G. Rogl, P. Rogl, M. Jain, S. Suwas and R.C. Mallik, *Acta Mater.*, **100**, 266, (2015).

[135] R. Chetty, D.S. Prem Kumar, G. Rogl, P. Rogl, E. Bauer, H. Michor, S. Suwas, S. Puchegger, G. Gieister and R.C. Mallik, *Phys. Chem. Chem. Phys*., **17**, 1716, (2015).

[136] D.S. Prem Kumar, R. Chetty, P. Rogl, G. Rogl, E. Bauer, P. Malar and R.C. Mallik, *Intermetallics*, **78**, 21, (2016).

[137] S. Harish, D. Sivaprahasam, M. Battabyal and R. Gopalan, *J. Alloy Compd*., **667**, 323, (2016).

[138] S-Y. Kim, G-E. Lee and I-H. Kim, *J. Korean. Phys. Soc*., **74**, 967, (2019).

[139] D.S. Prem Kumar, S. Tippireddy, A. Ramakrishnan, K-H. Chen, P. Malar, and R.C. Mallik, *Semicond. Sci. Technol.*, **34**, 035017, (2019).

[140] L.L. Huang, Y.S. Wang, C. Zhu, R. Xu, J.M. Li, J.H. Zhang, D. Li, Z.M. Wang, L. Wang, C.J. Song, H.X. Xin, J. Zhang and X.Y. Qin, *J. Alloy Compd*., **769**, 478, (2018).

[141] D.I. Nasonova, A.V. Sobolev, I.A. Presniakov, K.D. Andreeva and A.V. Shevelkov, *J. Alloy Compd*., **778**, 774, (2019).

[142] Y. Kosaka, K. Suekuni, K. Hashikuni, Y. Bouyrie, M. Ohta and T. Takabatake, *Phys. Chem. Chem. Phys*., **19**, 8874, (2017).

[143] P. Levinsky, C. Candolfi, A. Dauscher, B. Lenoir and J. Hejtmanek, *J. Electron. Mater.*, **48**, 1926, (2019).

[144] X. Lu, D.T. Morelli, Y. Xia and V. Ozolins, *Chem. Mater*., **27**, 408, (2015).

[145] X. Lu and D. Morelli, *J. Electron. Mater*., **43**, 1983, (2014).

[146] Y. Bouyrie, C. Candolfi, V. Ohorodniichuk, B. Malaman, A. Dauscher , J. Tobola and B. Lenoir, *J. Mater. Chem. C*, **3**, 10476, (2015).

[147] D.S. Prem. Kumar. R. Chetty, O.E. Femi, K. Chattopadhyay, P. Malar and R.C. Mallik, *J. Electron Mater*., **46**, 2616, (2017).

[148] Y. Bouyrie, S. Sassi, C. Candolfi, J.B. Vaney, A. Dauscher and B. Lenoir, *Dalton Trans*., **45**, 7294, (2016).

[149] Y. Bouyrie, C. Candolfi, J.B. Vaney, A. Dauscher and B. Lenoir, *J. Electron Mater.*, **45**, 1601, (2016).

[150] X. Lu, D.T. Morelli, Y. Wang, W. Lai, Y. Xia and V. Ozolins, *Chem. Mater*., **28**, 1781, (2016).

[151] X. Lu, W. Yao, G. Wang, X. Zhou, D. Morelli, Y. Zhang, H. Chi, S. Hui and C. Uher, *J. Mater. Chem. A*, **4**, 17096, (2016).

[152] S. Tippireddy, R. Chetty, K.K. Raut, M.H. Naik, O.K. Mukharjee, M. Jain, R. Nath, K. Wojciechowski and R.C. Mallik, *Phys. Chem. Chem. Phys*., **20**, 28667, (2018).

[153] T. Barbier, S. Rollin-Martinet, P. Lemoine, F. Gascoin, A. Kaltzoglou, P. Vaqueiro, A.V. Powell and E. Guilmeau, *J. Am. Ceram. Soc*., **99**, 51, (2016).

[154] K. Tatsuka and N. Morimoto, *Econ. Geol*., **72**, 258, (1977).

[155] T. Barbier, P. Lemoine, S. Gascoin, O.I. Lebedev, A. Kaltzoglou, P. Vaqueiro, A.V. Powell, R.I. Smith and E. Guilmeau, *J. Alloys Compd.*, **634**, 253, (2015).

[156] E. Lara-Curzio, A.F. May, O. Delaire, M.A. McGuire, X. Lu, C-Y. Liu, E.D. Case and D.T. Morelli, *J. Appl. Phys*., **115**, 193515, (2014).

[157] W. Lai, Y. Wang, D.T. Morelli and X. Lu, *Adv. Func. Mater*. **25**, 3648, (2015).

[158] T.P. Mishra, M. Koyano and Y. Oshima, *Appl. Phys. Express*, **10**, 045601, (2017).

[159] K Suekuni, C.H. Lee, H.I. Tanaka, E. Nishibori, A. Nakamura, H. Kasai, H. Mori, H. Usui, M. Ochi, T. Hasegawa, M. Nakamura, S. Ohira-Kawamura, T. Kikuchi, K. Kaneko, H.

Nishiate, K. Hashikumi, Y. Kosaka, K. Kuroki and T. Takabatake, *Adv. Mater*., **30**, 1706230, (2018).

[160] P. Vaqueiro, G. Guélou, A. Kaltzoglou, R.I. Smith, T. Barbier, E. Guilmeau and A.V. Powell, *Chem. Mater*., **29**, 4080, (2017).

[161] P. Lemoine, C. Bourgès. T. Barbier, V. Nassif, S. Cordier and E. Guilmeau, *J. Solid State Chem*., **247**, 83, (2017).

[162] Y, Bouyrie, C. Candolfi, A. Dauscher, B. Malaman and B. Lenoir, *Chem. Mater*., **27**, 8354, (2015).

[163] Y. Yan, H. Wu, G. Wang, X. Lu and X. Zhou, *Energy Storage Mater*., **13**, 127, (2018).

[164] R-Z Zhang, K. Chen, B. Du and M.J. Reece, *J. Mater. Chem. A*, **5**, 5013, (2017).

[165] H.J. Goldsmid, in *Thermoelectrics Handbook: Macro to Nano*, ed. D.M. Rowe, CRC Press, Boca Raton, Ch. 3, p. 19, (2006)

[166] P. Qiu, T. Mao, Z. Huang, X. Xia, J. Liao, M.T. Agne, M. Gu, Q. Zhang, D. Ren, S. Bai, X. Shi, G.J. Snyder and L. Chen, *Joule*, **3**, 1538, (2019).

[167] R. Chetty, Y. Kikuchi, Y. Bouyrie, P. Jood, A. Yamamoto, K. Suekuni and M. Ohta, *J. Mater. Chem. C*, **7**, 5184, (2019).

[168] X Lu and D.T. Morelli, *Phys. Chem. Chem. Phys*., **15**, 5762, (2013).

[169] D.J. James, X. Lu, D.T. Morelli and S.L. Brock, *ACS Appl. Mater. Interfaces*. **7**, 23623, (2015).

[170] D.P. Weller, D.L. Stevens, G.E. Kunkel, A.M. Ochs, C.F. Holder, D.T. Morelli and M.E. Anderson, *Chem,. Mater*., **29**, 1656, (2017).

[171] T. Barbier, P. Lemoine, S. Martinet, M. Eriksson, M. Gilmas, E. Hug, G. Guélou, P. Vaqueiro, A.V. Powell and E. Guilmeau, *RSC Adv*., **6**, 10044, (2016).